Efficient Control of Magnetic Fields in Single Atom Experiments

Paul Koschmieder

München 2019

Efficient Control of Magnetic Fields in Single Atom Experiments

Paul Koschmieder

Masterarbeit
an der Arbeitsgruppe von Prof. Dr. Harald Weinfurter
der Ludwig–Maximilians–Universität
München

vorgelegt von
Paul Koschmieder
aus Speyer

München, den 18.02.2019

Effiziente Kontrolle von magnetischen Feldern in Einzelatomexperimenten

Paul Koschmieder

Masterarbeit
an der Arbeitsgruppe von Prof. Dr. Harald Weinfurter
der Ludwig–Maximilians–Universität
München

vorgelegt von
Paul Koschmieder
aus Speyer

München, den 18.02.2019

Contents

1. Introduction

A significant advancement of insight into fundamental physical principles has been the successful development of quantum mechanics. Coming from the first theories formulated in the beginning the 20th century it has evolved into a multi faceted field of rapidly developing research in physics. Some applications of those fundamental principles are on the verge of becoming a technology with a broad range of applications. One unique feature of quantum mechanics is the concept of entanglement. For the description of a state of a multi particle system, it is not sufficient to describe each particle on its own, but it is necessary to describe the state of the system holistically. Entanglement can arise from interaction of particles with each other by direct interaction or mediated by exchange of e.g. photons. It can be verified by measurements that will show strong correlations between the outcomes that exceed every correlation that can be explained by classical physics.

As research has progressed over the last 50 years a large variety of entangled states can be generated experimentally in various quantum systems. A very intriguing example is the entanglement of a single atom with a single photon [4, 39, 41]. This system can represent a building block of a quantum network. In abstract terms such a network has to consist of nodes of quantum memories and quantum communication channels connecting the nodes. The atom-photon system offers both, as the atom is a massive particle that can be used to store quantum information while the photon is an ideal information carrier to a distant location. For connecting two atoms (i.e. two quantum memories) in order to form a simple quantum network consisting of two memories and a channel, different approaches can be taken. Either they can be interfaced by coherent absorption of a photon entangled to an atom by another (spatially separated) atom [28] or by employing the entanglement swapping protocol where the four particle state of two entangled atom-photon pairs is used. By projecting the photons onto a maximally entangled Bell-state, the atoms will be entangled [43].

Several interesting applications for quantum communication can be realized with entanglement over long distances. These include teleportation of quantum states between distant locations [3, 22, 36] and secure communication using quantum key distribution (QKD) [12]. The latter can also be performed in a device-independent way based on a loophole-free violation of Bell's inequality [1, 37, 2]. A common challenge is to increase the distance over which entanglement is distributed, typical demonstrations cover several meters, while there were demonstrations over several kilometers [22, 36]. To provide entanglement over longer distances the proposed quantum repeater [31] could be a solution.

One requirement that is common for all experiments of this kind is the coherence of the quantum memory. As all experimental processes take a finite amount of time the prepared quantum

state has to be preserved during the whole experimental procedure. Generally, the coherence of a quantum system depends on the level of its isolation from the environment, typical limiting factors being its interaction with electric, magnetic and optical fields. A common interface between memory and communication channel is the process of entangling a spin degree of freedom of the memory with the polarization degree of freedom of a photon. The spin degree of freedom of the memory is typically associated with with a finite magnetic moment making the system susceptible to magnetic fields which is a common limiting factor in such experiments [17].

The quantum system presented in this work consists of two neutral Rubidium 87 atoms trapped in individual traps at a distance of $400\,\mathrm{m}$. The atomic quantum systems are the nodes and memories of a simple quantum network, that are connected by a fiber link through which photons entangled to the atoms can be exchanged. By using the entanglement swapping protocol, the atoms are entangled. The procedure of entangling atoms at this distance takes time on the order of ten microseconds, during this time the atomic quantum state has to stay coherent. As the event rate of atom-atom entanglement events for the experimental setup presented here requires acquisition times of several hours to days, the precise stability of magnetic fields has to be achieved on that timescales as well and an efficient control and maintenance of the goodness of magnetic field control is key to experimental success. This can only be done by actual measurements on the atomic quantum states used as a memory and is therefore time consuming.

This thesis begins with a general introduction into basic principles and mechanisms used to entangle two atoms in remote traps in Chapter 2. In Chapter 3 the coherence properties of the atomic quantum state will be discussed, while Chapter 4 discusses the methods, achievements and limitations of the magnetic field compensation setup. The final Chapter 5 describes a method to efficiently control and calibrate the magnetic field compensation setup, leading to better state coherence during a long term experimental run.

2. Overview of the experiment

Creating entanglement between an atom and a photon and subsequently between an atom and another atom is a demanding task. Additionally, the large spatial separation of the two atoms imposes further obstacles. In the following chapter, I will outline some of the methods and techniques used to achieve atom-atom entanglement over the distance of $700\,\mathrm{m}$ (fiber length), thereby achieving a spatial separation of $398\,\mathrm{m}$. Even at this distance, an overall readout fidelity of 92% of the atomic states is achieved. This experimental setup was developed and built throughout the last 18 years with iterations on almost all the parts, described in detail in the according PhD theses done at this experiment [7, 16, 40, 24, 38, 29, 15, 20]. One major result achieved with this experimental setup was a statistically significant violation of Bell's inequality closing all essential loopholes, specifically closing the detection loophole and the locality loophole simultaneously [30].

2.1. Atomic quantum system

The quantum system used in this experiment is a single, neutral Rubidium-87 atom. There are several reasons why this is a preferable choice. ^{87}Rb is a alkaline atom, meaning that it has only one valence electron. Therefore the electronic band structure is fairly simple and well understood[34]. Furthermore the transitions are accessible with commercially available laser systems. According to the band structure calculations, the ground state of ^{87}Rb is $5S$ and the first excited state is $5P$. A level diagram of the electronic states relevant for this experiment is shown in Fig. 2.1. Due to the coupling of orbital angular momentum L and spin S of the valence electron, the first excited state has a fine structure splitting into two sub-levels, $5^2P_{3/2}$ and $5^2P_{1/2}$. These electronic levels are further split up by the hyperfine splitting. It arises from the coupling of the total angular momentum $J = L + S$ of the valence electron to the nuclear spin $I = \frac{3}{2}$ of ^{87}Rb. The ground state $5^2S_{1/2}$ splits into two hyperfine states, $F = 1$ and $F = 2$, whereas the relevant splitting of the excited states is denoted as F'. Those hyperfine states are subdivided into Zeeman states with the quantum number m_F. Those Zeeman states are degenerate in absence of external fields. Optical as well as magnetic fields will lift this degeneracy. As an atomic qubit, the Zeeman states $m_F = \pm 1$ of the ground state $5^2S_{1/2}$, $F = 1$ are chosen. Here the state $|F = 1, m_F = -1\rangle_z$ corresponds to $|\downarrow\rangle_z$ and $|F = 1, m_F = +1\rangle_z$ corresponds to $|\uparrow\rangle_z$. In order to achieve atom-photon entanglement, a Λ-system is necessary. Therefore the state $5^2P_{3/2}$, $F' = 0$ is used as the excited state to complete the Λ-system in addition to the two qubit states $|\downarrow\rangle_z$ and

$|\uparrow\rangle_z$. On top of that, the transition from $5^2S_{1/2}$, $F = 2$ to $5^2P_{3/2}$, $F' = 3$ is a closed transition allowing for efficient laser cooling.

2.2. Lasers and vacuum

In technical terms ^{87}Rb is a preferable choice, because there is a high availability of commercial products to do optical manipulations on the ^{87}Rb quantum system. Especially for the D1-line at 780 nm and the D2-line at 795 nm, there are a lot of easy to access commercial optical components, such as fibers, beam splitters, mirrors and lenses. As laser light sources to address those transitions, commercial grating-stabilized diode lasers[1] are used. To stabilize their frequency on the D1-line and respectively the D2-line, the laser diodes run on an external resonator created by a actively controlled grating. The grating is inside a feedback loop that uses a signal from Doppler-free saturation spectroscopy of Rubidium to act as a frequency lock. For addressing different hyperfine states of the atom, acousto-optical modulators (AOMs) are used to fine-tune the light frequency.

In order to work with a quantum system that is sufficiently isolated from the environment, it is necessary to perform those experiments under ultra-high vacuum (UHV) conditions, meaning pressures below 10^{-9} mbar. This is achieved in a vacuum chamber where low pressure is maintained by an ion-getter pump[2]. Attached to the vacuum chamber is a glass cell, where the atom trap is located. As the trapping and manipulation of the atom is purely done with light, the glass cell provides optical access to the atom from most directions. The rubidium for the experiment is introduced to the vacuum by a metal vapor dispenser. This is a small tube which is electrically heated to achieve temperatures at which the amount of rubidium needed for the experiment is evaporated. As the experiment has been running for years, some of the rubidium initially evaporated by the vapor dispenser has precipitated on the walls of the vacuum glass cell, therefore it is also possible to vaporize this rubidium again by shining on it with a light-emitting diode in the ultraviolet spectral range.

2.3. Trapping

To perform well-controlled operations on the atomic quantum system, the experiment requires a method to trap single neutral ^{87}Rb atoms, meaning that the position of the atom needs to be well defined within the time frame of the whole experimental procedure, in order to grant optical access to the atom during that time. Furthermore a strong localization is necessary to collect the fluorescence light emitted by the atom efficiently. In addition to that, the trapping mechanism must not lift the degeneracy of the Zeeman sublevels of one hyperfine state, as these

---

[1]Toptica DL pro
[2]Varian/Agilent Vaclon Plus 55 Starcell
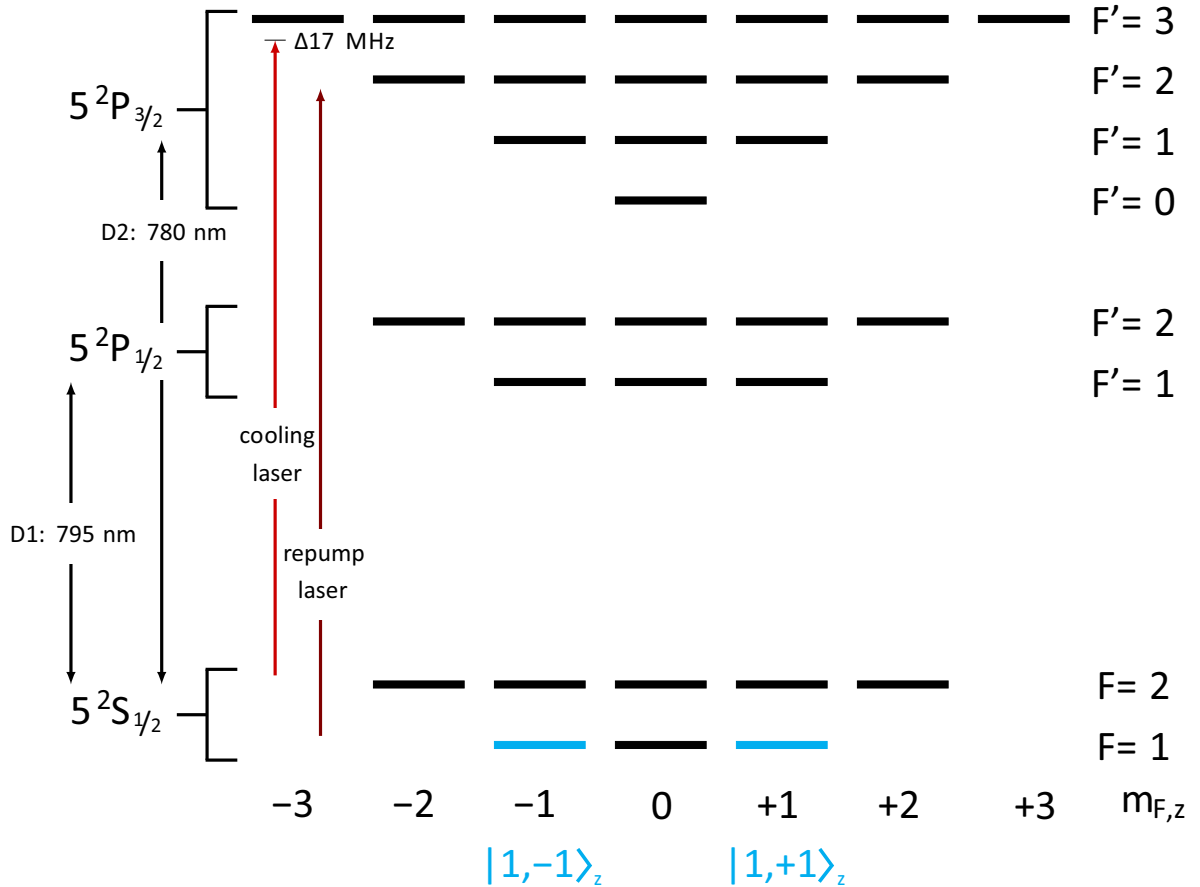
Figure 2.1.: Level scheme of ^{87}Rb [26]. The ground level $5^2S_{1/2}$ splits into hyperfine levels $F = 1$ and $F = 2$. The atomic qubit will be encoded in $|1, -1\rangle_z := |\downarrow\rangle_z$ and $|1, +1\rangle_z := |\uparrow\rangle_z$ of the $F = 1$ ground level as marked in blue. The state manifolds of $5^2P_{1/2}$ and $5^2P_{3/2}$ that can be addressed from the ground level with optical transitions driven by lasers with wavelength of 795 nm (D2-line) and 780 nm (D1-line) respectively. Also shown are the transitions used for the cooling cycle of the atom described in sec 2.3.2. [26]

are used to encode the qubit and should not be disturbed. These requirements can be met by a strongly focused optical dipole trap (ODT) [8], which will be introduced in this section. As the atoms introduced to the vacuum chamber are evaporated at room temperature and the ODT has a very shallow trapping potential on the order of $k_B \cdot 1$ mK, an intermediate cooling method is indispensable. Therefore Doppler cooling in a magneto-optical trap (MOT) is employed. The MOT is able to trap a cloud of many atoms and cool them to temperatures at around 30 μK (see sec. 5.1.4), which is well below the Doppler limit, which is at 146 μK [34]. At those temperatures it is possible to load a single atom into the ODT simply by spatially overlapping both traps. The following chapter will give a more detailed description of the trapping mechanisms used in this experiment.

2.3.1. Optical dipole trap (ODT)

The ODT is a simple method to trap a single, neutral atom. It uses a tightly focused Gaussian beam to create an attractive potential for the atoms. The underlying effect creating this attractive potential is the AC-Stark effect. If the beam is far detuned from a transition between a ground and a excited state, it shifts the eigenenergy of the ground state by:

$$\Delta E_g = \frac{\hbar \Omega^2}{4\Delta} \sim I \tag{2.1}$$

Here Ω is the on-resonance Rabi-frequency, which is proportional to the square root of the intensity I, whereas $\Delta = \omega_A - \omega_L$ is the detuning of the light field, i.e. the difference between the atomic transition frequency and the light field frequency. For the potential to be attractive, Δ is chosen to be negative. Additionally, the atom should remain in the ground state and undisturbed. Therefore the detuning is chosen to be large, which leads to the use of a far red-detuned light ($\Delta \gg 0$).

The spatial shape of the trap potential is given by the spatial intensity profile of the beam. In case of a focused Gaussian beam propagating along the z-axis, the intensity distribution looks like:

$$I(r, z) = I_0 \cdot \left(\frac{w_0}{w(z)}\right)^2 \cdot e^{-\frac{2r^2}{w(z)^2}} \tag{2.2}$$

Here I_0 is the maximal intensity and w_0 is the minimal transversal waist, both at $r = 0$ and $z = 0$. $w(z)$ is the transversal waist at a given position z along the propagation direction of the beam:

$$w(z) = w_0 \sqrt{1 + \left(\frac{z}{z_R}\right)^2} \tag{2.3}$$

where

$$z_R = \frac{\pi w_0^2}{\lambda} \tag{2.4}$$
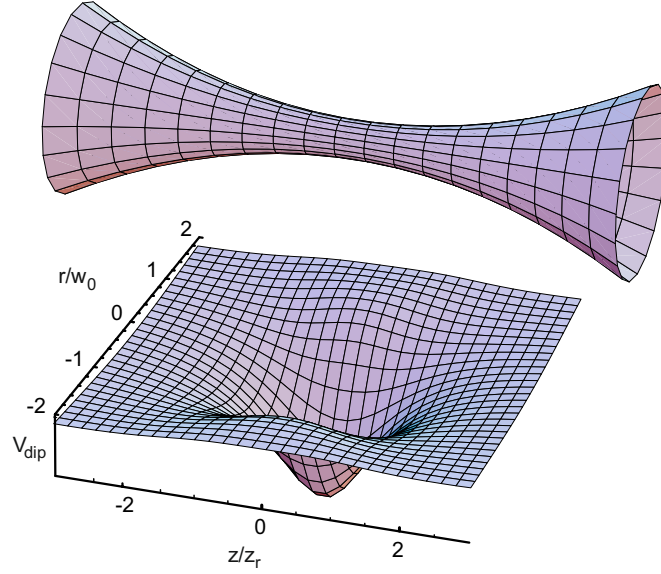
Figure 2.2.: Schematic visualization of a focused Gaussian beam and the resulting trapping potential for a far red-detuned beam. [40]

is the Rayleigh length and λ is the wavelength of the light. This results in a different trapping potential along the axis of propagation compared to the trapping potential in radial direction. A graphical representation of a focused Gaussian beam and the resulting trapping potential can be found in Fig. 2.2.

For the case of a ^{87}Rb atom, the level structure is far more complex than a two level system, but it can be well approximated by a three-level system with $5^2 S_{1/2}$ as ground state and $5^2 P_{3/2}$ and $5^2 P_{1/2}$ as excited states. Then the dipole trap potential for each Zeeman sub-state of the ground state $5^2 S_{1/2}$ looks like [13]:

$$U_{dip}(r,z) = \Delta E(r,z) = \frac{\pi c^2 \Gamma}{2\omega_0^3} \cdot \left(\frac{2 + P g_F m_F}{\Delta_{2,F}} + \frac{1 - P g_F m_F}{\Delta_{1,F}} \right) \cdot I(r,z) \qquad (2.5)$$

where Γ and ω_0 are the spontaneous decay rate and the central transition frequency of the D-line, g_F the Landé-factor of the according Zeeman-state m_F, $\Delta_{1,F}$ and $\Delta_{2,F}$ are the detunings of the light field relative to the D1-line and D2-line and P the polarization of the light ($P = \pm 1$ for circular polarization and $P = 0$ for linear polarization). This results in a trap depth of $U_0 \sim I_0$. A further approximation that is well justified is to assume the trapping potential to be harmonic, as the thermal energy of the atom is much smaller than the trap depth ($k_B T \ll U_0$) [40]. Therefore

the trapping frequencies are given by:

$$\Omega_r = \sqrt{\frac{4U_0}{m_{Rb}w_0^2}}$$

$$\Omega_z = \sqrt{\frac{2U_0}{m_{Rb}z_R^2}} \tag{2.6}$$

where Ω_r is the trapping frequency in radial direction, Ω_z is the trapping frequency in axial direction and m_{Rb} is the mass of the ^{87}Rb atom.

This scheme presents an attractive potential to all ^{87}Rb atoms. But as demonstrated in [33, 32], by choosing the trap depth and the trap size correctly (typically $w_0 < 4\,\mu$m), there is a collisional blockade mechanism. Within this mechanism, atoms in the excited state collide and will eventually be lost from the trap. As the cooling light of the MOT will populate the excited state, this effect is already present during loading and atoms are expelled from the trap until there is only one atom left within the ODT.

2.3.2. Magneto optical trap (MOT)

In order to be able to trap a single atom with an ODT, their kinetic energy needs to be below the level of the ODT trap depth. This is initially not the case, as the atoms are introduced to the experiment by a vapor dispenser at room temperature (300 K). Therefore the atoms need to be cooled. This can be done by radiation pressure using the Doppler effect [14, 9]. Six beams from all spatial directions each form pairs of counter-propagating beams, that are red-detuned by 17 MHz with respect to the atomic transition from $5^2S_{1/2}$, $F = 2$ to $5^2P_{3/2}$, $F' = 3$ (see Fig. 2.1). As an atom moves along a certain direction, the detuning of the beam propagating against the direction of the atom movement is reduced due to the Doppler effect. Therefore the atom will scatter more photons from this beam. While the momentum transfer of the absorption process is directed contrary to the atom movement, the emission is isotropic. This creates a net momentum transfer contrary to the atom movement and thereby a velocity dependent force which decelerates the atoms. As the the atoms undergo this cooling cycle many times, some decay to the $5^2S_{1/2}$, $F = 1$ state. In order to get hold of those atoms, there is a repump laser beam that drives the transition from $5^2S_{1/2}$, $F = 2$ to $5^2P_{3/2}$, $F' = 3$ and thereby puts those atoms back into the cooling cycle. In order to add to the velocity dependent force a position dependent force that traps the atoms at the correct position overlapped with the ODT, a magnetic quadrupole field is applied. It is generated by two coils in anti-Helmholtz configuration placed outside the glass cell. The center of the quadrupole field is overlapped with the intersection of the cooling beams. In that way and by choosing the appropriate polarization of the cooling beams, atoms that move away from the trap center experience a shift in their Zeeman sub-states resulting in a net radiation pressure pushing them back to the center. With this process temperatures even below the Doppler limit of 146 μK [34] can be reached due to polarization gradient cooling [11]. The limit that can be achieved in our setup is at around 30 μK (see sec. 5.1.4)
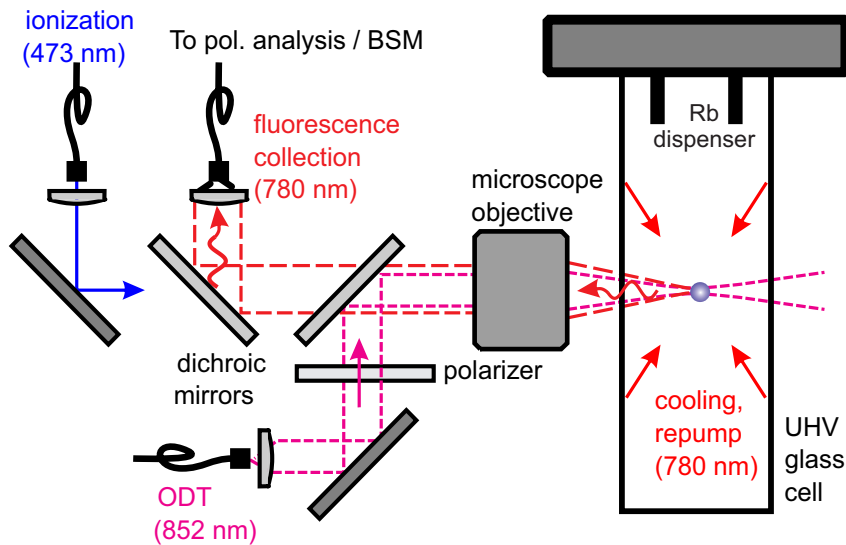
Figure 2.3.: Setup of the confocal microscope objective, which is used to create the dipole trap and simultaneously collect fluorescence of the atom in the trap. The collected fluorescence is coupled into a single mode fiber and send to a polarization analysis apparatus counting with single photon precision. Additionally the light pulse used for ionizing the atom during state readout is also sent through this objective. [19]

2.3.3. Confocal microscope setup

A unique feature of this experiment is the use of a confocal microscope objective, that serves for three purposes at the same time. One the one hand, it is used as the objective to tightly focus a laser beam, which creates the ODT. The beam with a wavelength of 852 nm is in a Gaussian mode and focused to a waist of $w_0 = 1.92$ µm, creating the tight trapping potential for a single atom. On the other hand, the same objective acts as the collection optics for the fluorescence light emitted by the atom. As the fluorescence is used to determine whether an atom is in the trap or not and for doing atom-photon entanglement experiments, it is crucial that the fluorescence collection is as efficient as possible. Therefore the focus of the dipole trap beam, i.e. the position of the atom and the focus for 780 nm light, being the wavelength of fluorescence emission, are chosen to precisely overlap. The fluorescence light is separated from the dipole trap beam by a dichroic mirror, coupled into a single mode fiber and sent to single photon detectors (avalanche photo diodes (APDs)). Additionally a laser beam with a wavelength of 473 nm is focused by the microscope objective to the position of the atom. This beam is passing two dichroic mirrors in order to be focused by the objective. The 473 nm light is only used in short pulses during the atomic state readout (sec. 2.5) and tries to ionize the atom. A schematic of the confocal microscope setup can be found in figure 2.3.

$5^3P_{3/2}$ $F' = 0$ $|0,0\rangle$

$|\sigma^+\rangle$ excitation $|\sigma^-\rangle$

$|\pi\rangle$

$5^2S_{1/2}$ $F = 1$

$|1,-1\rangle$ $|1,0\rangle$ $|1,+1\rangle$
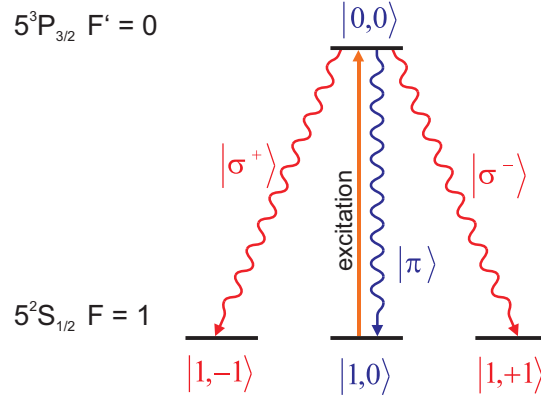
Figure 2.4.: Atom-photon entanglement scheme: excitation to $5^2P_{3/2}$, $F' = 0$, $m_{F'} = 0$ and subsequent spontaneous decay of the excited state back to $5^2S_{1/2}$, $F = 1$ state manifold, while sending out either a σ^+-, a σ^-- or a π-polarized photon. The π-polarized photon is not collected by the experiment due to the orientation of the quantization axis.

2.4. Atom-Photon entanglement

Entanglement between an atom and a photon can be generated by spontaneous emission of a photon by an atom. In the case of this experiment, atom-photon entanglement is implemented by making use of the $5^2P_{3/2}$, $F' = 0$ state and the $5^2S_{1/2}$, $F = 1$ state manifold of ^{87}Rb [39, 38]. The procedure is as follows: First the atom is prepared in the $5^2S_{1/2}$, $F = 1$, $m_F = 0$ state by means of optical pumping. Then a resonant π-pulse of light with a wavelength of 780 nm will transfer the atom efficiently to the $5^2P_{3/2}$, $F' = 0$ state. This state has a lifetime of 26.2 ns and the atom spontaneously decays back to one of the three states of the $5^2S_{1/2}$, $F = 1$ state manifold. There are three possible final states of the atom $5^2S_{1/2}|F = 1, m_F = -1\rangle$, $|F = 1, m_F = 0\rangle$ and $|F = 1, m_F = +1\rangle$. Due to conservation of angular momentum during the process of spontaneous emission of a photon, there are accordingly three possible spin states of the photon $|\sigma^+\rangle$ $|\sigma^-\rangle$ and $|\pi\rangle$, corresponding to to left circular, right circular and linearly polarized light (see Fig. 2.4). Each atomic state is thereby precisely mapped to exactly one polarization state of the emitted photon. As the spatial emission characteristics of $\sigma^\pm$- and π-polarized photons are different in such a way, that no π-polarized light can be coupled into the single mode fiber along the quantization axis (i.e. the optical axis of the confocal microscope setup), only $\sigma^\pm$-polarized photons are coupled into the single mode fiber and thereby recognized as events by the experiment. Therefore the resulting entangled atom-photon state, that can be

recognized by the experiment is

$$|\Psi\rangle_{a,p} = \frac{1}{\sqrt{2}} \left(|\sigma^+\rangle \, |\downarrow\rangle_z + |\sigma^-\rangle \, |\uparrow\rangle_z \right) \tag{2.7}$$

$$= \frac{1}{\sqrt{2}} \left(|H\rangle \, |\downarrow\rangle_x + |V\rangle \, |\uparrow\rangle_x \right)$$

$$= \frac{1}{\sqrt{2}} \left(|+\rangle \, |\downarrow\rangle_y + |-\rangle \, |\uparrow\rangle_y \right).$$

Definitions of reference frames and qubit basis transformations can be found in equation A.1 Atom-photon entanglement can be characterized by measuring correlations between the atomic spin and the photonic polarization state in different basis sets.

2.5. Atomic state readout

In order to characterize atom-photon entanglement, the experiment requires a method to read out the electronic state of the atom. Therefore a read out method that can distinguish the Zeeman states of the $5^2S_{1/2}$, $F = 1$ state manifold is needed. The method also needs to be capable of reading out the atomic Zeeman state in any basis, to not only show correlation, but rather characterize entanglement. These requirements can be met by a Zeeman state-selective ionization scheme.

As shown in Fig. 2.5, the state readout consists of three laser pulses. As the atomic state before readout is some kind of superposition state in the $5^2S_{1/2}$, $F = 1$ state manifold, the readout laser pulse ($\lambda = 795\,\text{nm}$) will create a bright state $|\Psi_B\rangle$ and an orthogonal dark state $|\Psi_D\rangle$ due to its polarization. An example therefor would be a readout beam with σ^+- polarization (see Fig. 2.5). As the atomic qubit is encoded in the states $|m_F = \pm 1\rangle_z$ of $5^2S_{1/2}$, $F = 1$, the readout pulse will transfer $|m_F = -1\rangle_z$ to $5^2P_{1/2}$, $F' = 1$, $m_F = 0$, whereas there is no transition possible for $|m_F = +1\rangle_z$ due to dipolar selection rules. Hereby $|m_F = -1\rangle_z$ is the bright state to the σ^+- polarized readout pulse and $|m_F = +1\rangle_z$ is the dark state. Generally speaking, the choice of a polarization $|\chi\rangle$

$$|\chi\rangle_{ro} = \cos(\alpha) \, |V\rangle + e^{i\phi} \sin(\alpha) \, |H\rangle \tag{2.8}$$

with angles α and ϕ creates a dark and a bright state for any atomic qubit state according to

$$|\Psi_B\rangle = \sin(\alpha) \, |\uparrow\rangle_x - e^{i\phi} \cos(\alpha) \, |\downarrow\rangle_x \tag{2.9}$$

$$|\Psi_D\rangle = \cos(\alpha) \, |\uparrow\rangle_x + e^{i\phi} \sin(\alpha) \, |\downarrow\rangle_x \tag{2.10}$$

where $|\uparrow\rangle_x = \frac{1}{\sqrt{2}} \left(|\uparrow\rangle_z + |\downarrow\rangle_z \right)$ and $|\downarrow\rangle_x = \frac{i}{\sqrt{2}} \left(|\uparrow\rangle_z - |\downarrow\rangle_z \right)$. For further relations between atomic and photonic states see appendix A. Due to those relations, an atomic state readout with an arbitrary basis is possible by choosing the polarization of the readout laser pulse. If the atom is transferred to the $5^2P_{1/2}$, $F' = 1$, $m_F = 0$ state, it will be ionized by a $473\,\text{nm}$ laser that is

Table 2.1.: Polarization of the readout laser pulse $|\chi\rangle_{ro}$ and resulting bright state $|\Psi_B\rangle$ and dark state $|\Psi_D\rangle$ of the atom.

$|\chi\rangle_{ro}$	$|\Psi_B\rangle$	$|\Psi_D\rangle$
$|L\rangle$	$|1,-1\rangle_z$	$|1,+1\rangle_z$
$|R\rangle$	$|1,+1\rangle_z$	$|1,-1\rangle_z$
$|H\rangle$	$\frac{i}{\sqrt{2}}\left(|1,-1\rangle_z - |1,+1\rangle_z\right)$	$\frac{1}{\sqrt{2}}\left(|1,-1\rangle_z + |1,+1\rangle_z\right)$
$|V\rangle$	$\frac{1}{\sqrt{2}}\left(|1,-1\rangle_z + |1,+1\rangle_z\right)$	$\frac{i}{\sqrt{2}}\left(|1,-1\rangle - |1,+1\rangle_z\right)$
$|+\rangle$	$\frac{1}{\sqrt{2}}e^{-i\frac{\pi}{4}}\left(i\,|1,-1\rangle_z + |1,+1\rangle_z\right)$	$\frac{1}{\sqrt{2}}e^{i\frac{\pi}{4}}\left(i\,|1,-1\rangle_z - |1,+1\rangle_z\right)$
$|-\rangle$	$\frac{1}{\sqrt{2}}e^{i\frac{\pi}{4}}\left(i\,|1,-1\rangle_z - |1,+1\rangle_z\right)$	$\frac{1}{\sqrt{2}}e^{-i\frac{\pi}{4}}\left(i\,|1,-1\rangle_z + |1,+1\rangle_z\right)$

focused on the atom during state readout, meaning that the atomic system will be split up into ionization fragments, i.e. an electron and an ion. As the ionization process should be as efficient as possible to guarantee a good readout fidelity, an additional cycling laser pulse illuminates the atom. This pulse re-excites possible decays from the excited state to $5^2S_{1/2}$, $F = 2$ back to $5^2P_{3/2}$, $F' = 3$, for the atom to still be ionized. As the ionization fragments are not trapped by the ODT, they are lost from the trap. To verify whether the atom is still in the trap (or not) after a ionization try, cooling and repump light can be shone onto the trap. If an atom is still there, it will fluoresce and the fluorescence can be collected by the collection optics and quantified on the single photon detectors (see Fig. 2.3). If the trap is empty, we will only see residual background counts on the single photon detectors. This method takes about 66ms [24], which is needed to collect enough fluorescence light to determine whether the atom is still in the trap or not.

The method mentioned above was too slow for the loophole free test off Bell's inequality. Therefore a much faster scheme to detect the ionization fragments was developed [24, 15, 30]. There, the possible ionization fragments are detected by two Channel Electron Multipliers (CEMs). To achieve a measurable electric signal, the ionization fragments are accelerated towards the CEMs by a strong electric field. As a fragment hits the active area of a CEM, secondary electrons are released and create an avalanche of electrons in the back part of the CEM, which in the end results in a small current pulse. There are two ionization fragments, but it is sufficient to only recognize one fragment to register a successful ionization event. This results in a combined detection efficiency of the CEMs of $\eta \gtrsim 0.98$. Further limits to the performance of the atomic state readout scheme are events where the atom was ionized despite being in a dark state, or vice versa not being ionized while being in a bright state (for details see [24]). It results in a total contrast of distinguishing bright state from dark state for the state-selective ionization scheme of 93.8%.
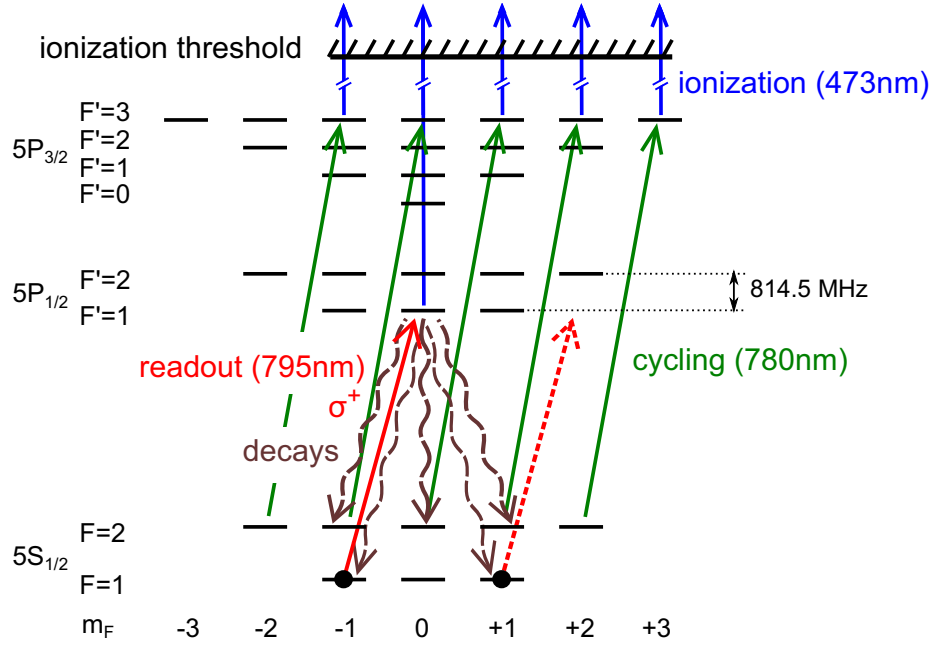
Figure 2.5.: Scheme for atomic state readout. The polarization of the readout laser (here σ^+) determines bright state (here $5^2S_{1/2}$, $F = 1$, $m_F = -1$) and dark state (here $5^2S_{1/2}$, $F = 1$, $m_F = +1$) of Zeeman state selective ionization. Additionally, the cycling laser re-excites atoms which decayed in certain channels before ionization. [19]

2.6. Atom-photon correlation measurements

With the methods mentioned above in place, an experiment to perform is to measure the correlations between the polarization state of the photon and the spin state of the atom, that are entangled. To perform such an experiment initially an atom needs to be trapped in the optical dipole trap (ODT). After preparing the state of the atom in $5^2S_{1/2}$, $F = 1$, $m_F = 0$, the atom-photon entanglement is initialized by sending the excitation pulse. The procedure of pumping and exciting the atom is repeated until a photon is collected by the collection optics and registered at one of the two single photon detectors (APDs) in a predefined time window after polarization analysis of the photon. As the overall photon detection efficiency is only at about $1.6 \cdot 10^{-6}$, this process of pumping and exciting the atom has to be repeated often. The polarization analysis consists of a rotatable quarter wave plate and a rotatable half wave plate in front of a polarizing beam splitter, all placed in front of the APDs, which allows a polarization measurement in an arbitrary basis. If a photon is registered, the experiment immediately switches to the atomic state readout scheme (see Fig. 2.6). The result of many such events allows us to calculate a state population of the dark state $|\Psi_D\rangle$ chosen by the readout polarization $|\chi\rangle_{ro}$ for a given basis of the photon polarization state analysis (e.g. $|H\rangle/|V\rangle$ or $|+\rangle/|-\rangle$). To verify entanglement, correlation curves for two photonic bases are measured. The readout polarization $|\chi\rangle_{ro}$ is rotated for each

Table 2.2.: Fit parameters for measurements in fig. 2.7 [7]

photonic state	A	$\Delta\phi\,(°)$	c
$|V\rangle$	0.939 ± 0.0050	2.85 ± 0.170	0.038 ± 0.0034
$|H\rangle$	0.905 ± 0.0064	0.65 ± 0.224	0.050 ± 0.0037
$|-\rangle$	0.926 ± 0.0069	1.08 ± 0.193	0.045 ± 0.0042
$|+\rangle$	0.914 ± 0.0086	2.69 ± 0.245	0.050 ± 0.0052
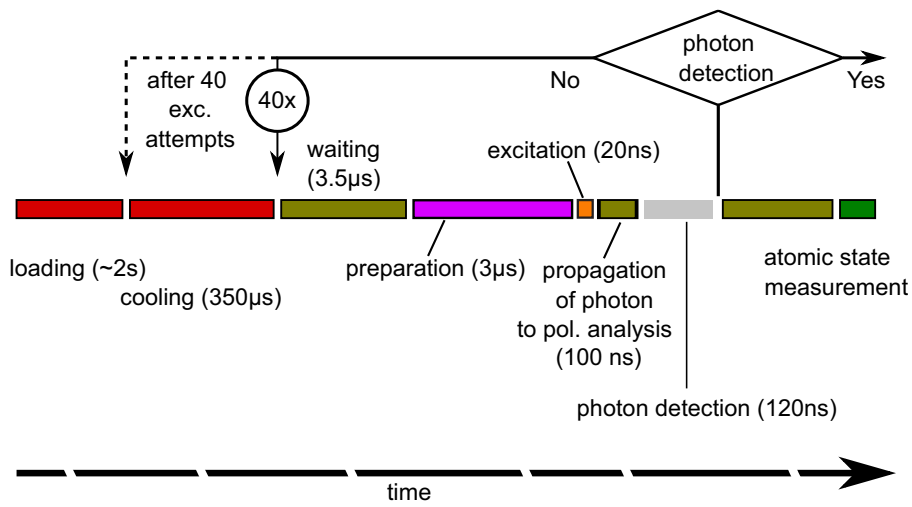
Figure 2.6.: Experimental sequence to entangle the spin state of a ^{87}Rb atom with the polarization state of a photon. After loading an atom in the dipole traps, the pumping and excitation scheme is repeated to create atom-photon entanglement by spontaneous emission. If a photon is measured after polarization analysis, the setup switches to atomic state analysis.

setting. A measurement of this kind is shown in Fig. 2.7. The results can be fitted by

$$f(\alpha) = A \sin^2(\alpha - \phi) + c \tag{2.11}$$

where A is the peak-to-peak amplitude, ϕ is the phase and c the offset. The amplitude A is the contrast of the entangled state, while the offset c should be 0 and is (together with A) a figure of merit for the state analysis. the phase ϕ should be 0 for detected photonic state $|V\rangle$, $\frac{\pi}{2}$ for $|H\rangle$, $\frac{\pi}{4}$ for $|+\rangle$ and $-\frac{\pi}{4}$ for $|-\rangle$. The difference from these expected values is $\Delta\phi$ and should be 0. These fitted coefficients displayed in table 2.2 give an overview of the performance of the entanglement and the readout scheme for atom-photon entanglement, which sets boundaries on the achievable correlations of atom-atom entanglement, which will be discussed in the following section.

(a) Photonic states $|H\rangle$ and $|V\rangle$ (b) Photonic states $|+\rangle$ and $|-\rangle$
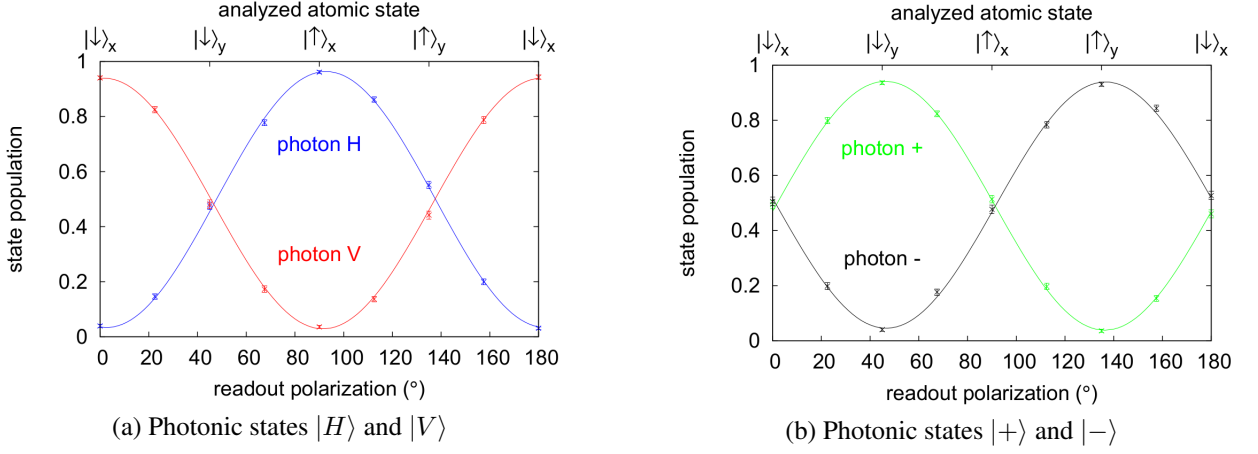
Figure 2.7.: Measurement of correlation of photonic and atomic state with minimal time delay between photonic and atomic state measurement ($0.4\,\mu s$). Shown is the dark state population for different angles of linearly polarized readout light ($|\chi\rangle_{ro} = |V\rangle \mathrel{\hat{=}} 0°$). Additionally shown are fits of the correlations according to (2.11). [7]

2.7. Atom-atom entanglement

In order to generate entanglement between two atoms with large spatial separation, the experiment employs the entanglement swapping protocol [43, 25]. This protocol opens up the possibility to entangle two atoms not by direct (contact) interaction, but instead uses two atom-photon pairs, where each atom-photon pair is entangled initially. After independent generation of two entangled atom-photon pairs, the photons are overlapped and projected onto an entangled state themselves, thereby entangling the atoms. The initial joint four-particle state of two entangled atom-pairs can be written as

$$|\Psi\rangle = |\Psi\rangle_{a1,p1} \otimes |\Psi\rangle_{a2,p2}$$

$$|\Psi\rangle = \frac{1}{2}\left(|\uparrow\rangle_{x,1}|H\rangle_1 + |\downarrow\rangle_{x,1}|V\rangle_1\right) \otimes \left(|\uparrow\rangle_{x,2}|H\rangle_2 + |\downarrow\rangle_{x,2}|V\rangle_2\right) \tag{2.12}$$

where ($|\uparrow\rangle_{x,1/2}$, $|\downarrow\rangle_{x,1/2}$) is the atomic qubit basis and ($|H\rangle_{1/2}$, $|V\rangle_{1/2}$) is the photonic basis. Projecting the photons onto a Bell state yields four possible outcomes, which are the four maximally entangled Bell states $|\Phi^\pm\rangle_{p1,p2} = \frac{1}{\sqrt{2}}\left(|HH\rangle \pm |VV\rangle\right)$ and $|\Psi^\pm\rangle_{p1,p2} = \frac{1}{\sqrt{2}}\left(|HV\rangle \pm |VH\rangle\right)$. Expanding and ordering (2.12) by possible outcomes of a photon projection yields

$$|\Psi\rangle = \frac{1}{2}\left(|\Psi^+\rangle_{a1,a2}|\Psi^+\rangle_{p1,p2} + |\Psi^-\rangle_{a1,a2}|\Psi^-\rangle_{p1,p2} + |\Phi^+\rangle_{a1,a2}|\Phi^+\rangle_{p1,p2} + |\Phi^-\rangle_{a1,a2}|\Phi^-\rangle_{p1,p2}\right)$$

This shows that the detection of a photonic Bell state projects the atoms onto the according Bell state $|\Phi^\pm\rangle_{a1,a2} = \frac{1}{\sqrt{2}}\left(|\uparrow\uparrow\rangle_x \pm |\downarrow\downarrow\rangle_x\right)$ or $|\Psi^\pm\rangle_{a1,a2} = \frac{1}{\sqrt{2}}\left(|\uparrow\downarrow\rangle_x \pm |\downarrow\uparrow\rangle_x\right)$.
The projection of the photonic state onto a Bell state takes place in a dedicated measurement apparatus. It consists of a non-polarizing 50/50 fiber beamsplitter followed by two polarizing beam
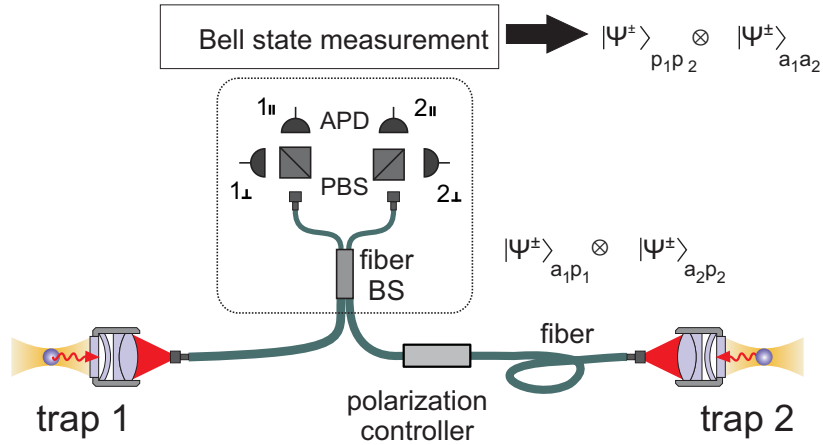
Figure 2.8.: Scheme for atom-atom entanglement. Atom-photon entanglement is created in two separate traps, followed by a Bell state measurement on the two photons (coincidental detection of two photons). Thereby atom-atom entanglement is created according to the entanglement swapping protocol without any direct interaction between the atoms. [19]

splitters (PBS) and four single-photon detectors (APDs) as shown in Fig. 2.8. On the initial fiber beam splitter, the photons interfere and experience the Hong-Ou-Mandel effect[18]. It is crucial that the photons are indistinguishable, i.e. they have to be in the same quantum state concerning all their degrees of freedom except their polarization. As the photons in this experiment come from the identical atomic transition and the photon generation in both traps is synchronized in time, the overlap of the spectral and temporal mode of the photons is close to unity. As this is the case, the Hong-Ou-Mandel effect leads to bunching or antibunching of the photons at the fiber beam splitter according to the symmetry of the two photon state.

Afterwards the two PBS analyze the polarization state of the photons. The photons are then recognized by the according APD. By registering coincidental clicks on APDs $1_\parallel \wedge 2_\perp$ or $1_\perp \wedge 2_\parallel$ the photonic state is determined to be $|\Psi^-\rangle$, whilst registering clicks $1_\parallel \wedge 1_\perp$ or $2_\perp \wedge 2_\parallel$ projects the photons onto $|\Psi^+\rangle$. If such photonic events are registered, the two atoms are entangled accordingly with states $|\Psi^-\rangle_{a1,a2}$ or $|\Psi^+\rangle_{a1,a2}$. $\left|\Phi_{a1,a2}^\pm\right\rangle$ cannot be distinguished and corresponding events are ignored. The photonic measurement result heralds entanglement of the atoms. With this scheme a violation of Bell's inequality was demonstrated whilst simultaneously closing the locality and detection loophole [30].

One limit to this scheme is, that the procedure to entangle two atoms takes some time, as the traps are separated by $700\,\mathrm{m}$ of optical fiber. Therefore it takes time for the photons to be detected by the Bell-state analysis and it also takes time to send back the result of the two-photon coincidence measurement to the individual traps (for details see Fig. 2.9). For the atom-atom entanglement to still be valid, each atom needs to preserve its exact quantum state, whilst still being trapped in the ODT. This is called atomic state coherence and plays a crucial role in the strength of measurable correlation between the states of the two atoms. For the experimental setup as of today, the coherence time required is at least at $3.8\,\mu\mathrm{s}$ and $7.3\,\mu\mathrm{s}$, which corresponds
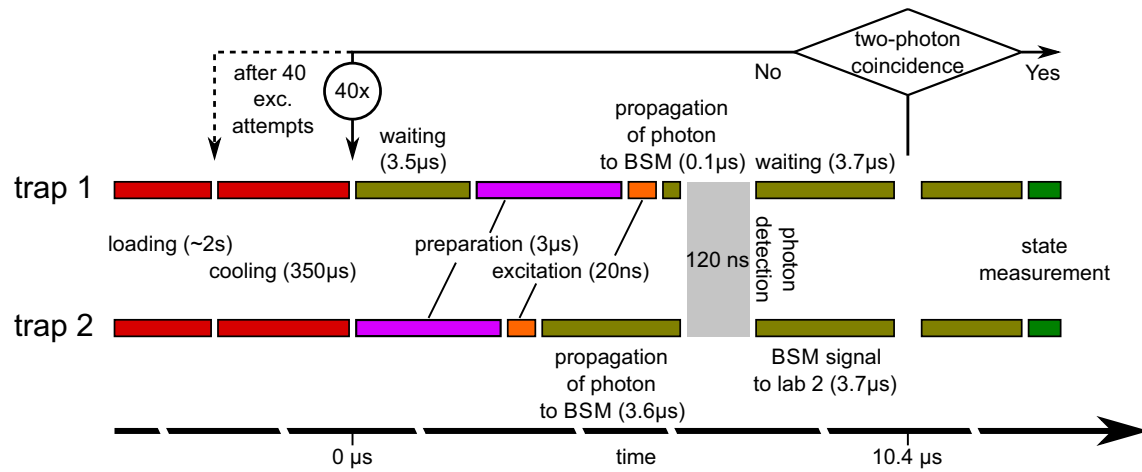
Figure 2.9.: Experimental sequence to entangle two ^{87}Rb atoms in two spatially separated traps. After successfully loading two atoms in both dipole traps, the pumping and excitation scheme is repeated to create atom-photon entanglement individually in both traps. As each excitation cycle heats the atom, there will be a cooling period after 40 excitation repetitions. If a suiting two photon coincidence is measured, the setup switches to atomic state analysis. [7]

to the delay in the respective trap between atom-photon entanglement ('excitation' in Fig. 2.9) and the atomic state readout ('state measurement'). As it is planned to increase the distance of the traps from 700 m to approximately 20 km (fiber length), the time of atomic state coherence needs to be increased by a factor of around 10 and it needs to be maintained easily during the course of a whole experimental run, which might take up to a few weeks. The following chapter will give an overview of the effects limiting atomic state coherence. Then I will point out which measures are taken in the experiment to compensate for those effects and maintain coherence. In the end I want to introduce a scheme, how to optimize the compensation in a time- saving and automated way.

3. Coherence properties of the atomic spin-1 system

A challenging requirement for this experiment is the coherence of the atomic quantum state, while the entanglement swapping protocol is employed. Due to the single atom being trapped under ultrahigh vacuum conditions, the possibilities of the atom interacting with its environment are heavily reduced. But there are still some remaining effects, that will influence the atomic quantum system, finally leading to decoherence. In this chapter, I will give insight into the effect magnetic fields have on the atom, called Zeeman effect. I will introduce the influence, that the light of the optical dipole trap (ODT) has on the atom due to the AC-Stark effect and I will explain, what effects the strong focusing of the ODT in combination with the motion of the atom in the trap gives rise to.

3.1. Evolution of a spin-1 system in a static magnetic field

There is a time-dependent evolution of atomic (hyperfine) states when the atom is exposed to external magnetic fields due to the Zeeman effect. This effect shifts the hyperfine states' energies relative to each other, which leads to a time evolution of the hyperfine states called Larmor precession. The description here is following up on those presented in [29] and [7]. Up to this point, only the states used to encode the qubit, a superposition of $5^2S_{1/2} |F = 1, m_F = \pm 1\rangle_z$ (short: $|1, \pm 1\rangle_z$) were considered. At this point, we also have to take into account the state $|F = 1, m_F = 0\rangle_z$ (short: $|1, 0\rangle_z$), that completes the spin-1 ground level state manifold of $5^2S_{1/2}$, $F = 1$. The Hamiltonian that governs the interaction is

$$\hat{\mathcal{H}} = \frac{\mu_B g_F}{\hbar} \vec{B} \cdot \hat{\vec{F}} \tag{3.1}$$

where μ_B is the Bohr magneton, $g_F = -\frac{1}{2}$ is the Landé-factor of the $5^2S_{1/2}$, $F = 1$ ground level, $\vec{B}$ is the vector of the magnetic field and $\hat{\vec{F}}$ is the operator of (hyperfine) angular momentum, which for a spin-1 system is composed of

$$\hat{\vec{F}} = \begin{pmatrix} \hat{F}_x \\ \hat{F}_y \\ \hat{F}_z \end{pmatrix}$$

with

$$\hat{F}_x = \frac{1}{\sqrt{2}} \begin{pmatrix} 0 & 1 & 0 \\ 1 & 0 & 1 \\ 0 & 1 & 0 \end{pmatrix},$$

$$\hat{F}_y = \frac{i}{\sqrt{2}} \begin{pmatrix} 0 & -1 & 0 \\ 1 & 0 & -1 \\ 0 & 1 & 0 \end{pmatrix},$$

$$\hat{F}_z = \frac{1}{\sqrt{2}} \begin{pmatrix} 1 & 0 & 0 \\ 0 & 0 & 0 \\ 0 & 0 & -1 \end{pmatrix}$$

when expressed in the basis of $(|1, +1\rangle_z, |1, 0\rangle_z, |1, -1\rangle_z)$. For simplicity we can write for the magnetic field as

$$\vec{B} = B \left(b_x \vec{e}_x + b_y \vec{e}_y + b_z \vec{e}_z \right) \tag{3.2}$$

with B the magnitude of the magnetic field and b_x, b_y, b_z being normalized components ($\sqrt{b_x^2 + b_y^2 + b_z^2} = 1$). With these relations, we can express the Hamiltonian as

$$\hat{\mathcal{H}} = \mu_B g_F B \begin{pmatrix} b_z & \frac{1}{\sqrt{2}} (b_x - ib_y) & 0 \\ \frac{1}{\sqrt{2}} (b_x - ib_y) & 0 & \frac{1}{\sqrt{2}} (b_x - ib_y) \\ 0 & \frac{1}{\sqrt{2}} (b_x + ib_y) & -b_z \end{pmatrix}$$

also given in the basis of $(|1, +1\rangle_z, |1, 0\rangle_z, |1, -1\rangle_z)$. Due to the symmetry of the problem with a quantization axis (z-axis) and an otherwise radially symmetric problem, it makes sense to transform $\hat{\mathcal{H}}$ into cylindrical coordinates by setting

$$b_x = \sqrt{1 - b_z^2} \cos(\phi)$$
$$b_y = \sqrt{1 - b_z^2} \sin(\phi)$$
$$b_z = b_z$$

If we additionally define the Larmor frequency

$$\omega_L := \frac{\mu_B g_F}{\hbar} B, \tag{3.3}$$

we can rewrite the Hamiltonian as

$$\hat{\mathcal{H}} = \hbar \omega_L \begin{pmatrix} b_z & \frac{1}{\sqrt{2}} \sqrt{1 - b_z^2} e^{-i\phi} & 0 \\ \frac{1}{\sqrt{2}} \sqrt{1 - b_z^2} e^{i\phi} & 0 & \frac{1}{\sqrt{2}} \sqrt{1 - b_z^2} e^{-i\phi} \\ 0 & \frac{1}{\sqrt{2}} \sqrt{1 - b_z^2} e^{i\phi} & -b_z \end{pmatrix}.$$

This operator has eigenvectors

$$|\Phi_{+1}\rangle = \begin{pmatrix} \frac{1}{2}\left(1+b_z\right)e^{-i\phi} \\ \frac{1}{\sqrt{2}}\sqrt{1-b_z^2} \\ \frac{1}{2}\left(1-b_z\right)e^{i\phi} \end{pmatrix}$$

$$|\Phi_{0}\rangle = \begin{pmatrix} -\frac{1}{\sqrt{2}}\sqrt{1-b_z^2}e^{-i\phi} \\ b_z \\ \frac{1}{\sqrt{2}}\sqrt{1-b_z^2}e^{i\phi} \end{pmatrix}$$

$$|\Phi_{-1}\rangle = \begin{pmatrix} \frac{1}{2}\left(1-b_z\right)e^{-i\phi} \\ -\frac{1}{\sqrt{2}}\sqrt{1-b_z^2} \\ \frac{1}{2}\left(1+b_z\right)e^{i\phi} \end{pmatrix}$$

and with the corresponding eigenvalues being $+\hbar\omega_L$, 0, $-\hbar\omega_L$. Therefore the time evolution of the eigenvectors is given be the time evolution operator, implying

$$|\Phi_{+1}\rangle(t) = |\Phi_{+1}\rangle(t=0) \cdot e^{-i\omega_L t}$$
$$|\Phi_{0}\rangle(t) = |\Phi_{0}\rangle$$
$$|\Phi_{-1}\rangle(t) = |\Phi_{-1}\rangle(t=0) \cdot e^{+i\omega_L t}.$$

Any arbitrary state of the atom can be written as a superposition of the eigenstates of the Hamiltonian

$$|\Psi\rangle = c_{+1}|\Phi_{+1}\rangle + c_0|\Phi_0\rangle + c_{-1}|\Phi_{-1}\rangle$$

leading to a time evolution of this arbitrary state of

$$|\Psi\rangle(t) = c_{+1}|\Phi_{+1}\rangle(t=0) \cdot e^{-i\omega_L t} + c_0|\Phi_0\rangle + c_{-1}|\Phi_{-1}\rangle(t=0) \cdot e^{+i\omega_L t}$$

which entirely describes the dynamics, that an arbitrary quantum state of the atom in its ground level in an constant external magnetic field experiences.

In the following section, I will give examples of the influence of some specific magnetic fields on states of the atom that are regularly prepared in the experiment. It will illustrate a way how to measure and quantify this effect experimentally.

3.1.1. Measuring Larmor precession

In order to measure these dynamics of the atomic quantum state, a straight forward way is to employ a measurement of atom-photon correlation as described in sec. 2.6. In addition, we now delay the atomic state readout by a certain time t. During this delay time t, the quantum state of the atom can evolve due to Larmor precession. This scheme is advantageous, as it determines the initial quantum state of the atom to a very high degree, as the polarization measurement of

the photon is fast and precise and projects the atom into a well-known state up to the fidelity of the polarization state analysis.

For this measurement, the photons are typically analyzed in an *H/V* basis, which therefore projects the atom either on $|\Psi_V\rangle = \frac{1}{\sqrt{2}}(|1,+1\rangle_z + |1,-1\rangle_z)$ or $|\Psi_H\rangle = \frac{i}{\sqrt{2}}(|1,-1\rangle_z - |1,+1\rangle_z)$ according to (2.7) and (A.1). The polarization of the readout laser pulse is chosen according to table 2.1 to $|\chi\rangle_{ro} = |V\rangle$ to set $|\Psi_V\rangle = |\Psi_D\rangle$ the dark state and $|\Psi_H\rangle = |\Psi_B\rangle$ the bright state of the atomic state readout. As shown in Fig. 2.5, atoms in state $|1,0\rangle_z$ will also be ionized and contribute to the fraction in $|\Psi_B\rangle$. After a certain delay time t, the final atomic quantum state is analyzed by projecting it onto the dark state $|\Psi_D\rangle$ of the atomic state readout. For a measurement, the delay time t is scanned to unveil the dynamics of the atomic quantum system and a meaningful number of events is collected. A simulation that shows the expected results of such a measurement is shown in Fig. 3.1

Field in z-direction

If we assume a magnetic field that is oriented along the z-axis, setting $b_z = 1$ and $b_x = b_y = 0$ ($\phi = 0$), it follows that the eigenstates of the Hamiltonian are

$$|\Phi_{+1}\rangle = \begin{pmatrix} 1 \\ 0 \\ 0 \end{pmatrix}, \qquad |\Phi_0\rangle = \begin{pmatrix} 0 \\ 1 \\ 0 \end{pmatrix}, \qquad |\Phi_{-1}\rangle = \begin{pmatrix} 0 \\ 0 \\ 1 \end{pmatrix},$$

which lets us express $|\Psi_V\rangle$ and $|\Psi_H\rangle$ in terms of $|\Phi_i\rangle$:

$$|\Psi_V\rangle = \frac{1}{\sqrt{2}}(|1,-1\rangle_z + |1,+1\rangle_z) = \frac{1}{\sqrt{2}}(|\Phi_{-1}\rangle + |\Phi_{+1}\rangle)$$

$$|\Psi_H\rangle = \frac{i}{\sqrt{2}}(|1,-1\rangle_z - |1,+1\rangle_z) = \frac{i}{\sqrt{2}}(|\Phi_{-1}\rangle - |\Phi_{+1}\rangle)$$

leading to a time evolution of

$$|\Psi_V\rangle(t) = \frac{1}{\sqrt{2}}\left(|1,-1\rangle_z \cdot e^{i\omega_L t} + |1,+1\rangle_z \cdot e^{-i\omega_L t}\right)$$

$$|\Psi_H\rangle(t) = \frac{i}{\sqrt{2}}\left(|1,-1\rangle_z \cdot e^{i\omega_L t} - |1,+1\rangle_z \cdot e^{-i\omega_L t}\right).$$

As a measurement of those states is always a projection onto the dark state of the atomic state readout, the probability of finding an atom that was initially prepared in state $|\Psi_V\rangle/|\Psi_H\rangle$ after a delay time t in $|\Psi_D\rangle$ is

$$\langle\Psi_D|\,\Psi_V\rangle(t) = \frac{1}{2}\left(\langle 1,-1|_z + \langle 1,+1|_z\right)\left(|1,-1\rangle_z \cdot e^{i\omega_L t} + |1,+1\rangle_z \cdot e^{-i\omega_L t}\right) = \cos(\omega_L t)$$

$$\langle\Psi_D|\,\Psi_H\rangle(t) = \frac{i}{2}\left(\langle 1,-1|_z + \langle 1,+1|_z\right)\left(|1,-1\rangle_z \cdot e^{i\omega_L t} - |1,+1\rangle_z \cdot e^{-i\omega_L t}\right) = \sin(\omega_L t)$$

$$P\left(|\Psi_D\rangle_V, t\right) = \|\langle\Psi_D|\ \Psi_V\rangle\left(t\right)\|^2 = \cos^2\left(\omega_L t\right) \tag{3.4}$$
$$P\left(|\Psi_D\rangle_H, t\right) = \|\langle\Psi_D|\ \Psi_H\rangle\left(t\right)\|^2 = \sin^2\left(\omega_L t\right).$$

This shows the Larmor precession with a period $T = \frac{\pi}{\omega_L}$. A pictorial display of such a state evolution can be found in Fig. 3.1.

Field in x-direction

For a field oriented along the x-axis, indicating $b_x = 1$, $b_y = b_z = 0$ and $\phi = 0$, the eigenstates of the Hamiltonian become

$$|\Phi_{+1}\rangle = \begin{pmatrix} \frac{1}{2} \\ \frac{1}{\sqrt{2}} \\ \frac{1}{2} \end{pmatrix}, \qquad |\Phi_0\rangle = \begin{pmatrix} \frac{-1}{\sqrt{2}} \\ 0 \\ \frac{1}{\sqrt{2}} \end{pmatrix}, \qquad |\Phi_{-1}\rangle = \begin{pmatrix} \frac{1}{2} \\ \frac{-1}{\sqrt{2}} \\ \frac{1}{2} \end{pmatrix}.$$

Again we can express $|\Psi_V\rangle$ and $|\Psi_H\rangle$ in terms of $|\Phi_i\rangle$, resulting in

$$|\Psi_V\rangle = \frac{1}{\sqrt{2}}\left(|1,-1\rangle_z + |1,+1\rangle_z\right) = \frac{1}{\sqrt{2}}\left(|\Phi_{-1}\rangle + |\Phi_{+1}\rangle\right)$$
$$|\Psi_H\rangle = \frac{i}{\sqrt{2}}\left(|1,-1\rangle_z - |1,+1\rangle_z\right) = i\,|\Phi_0\rangle.$$

These states show a time evolution of

$$|\Psi_V\rangle\left(t\right) = \cos\left(\omega_L t\right)|\Psi_V\rangle - i\sin\left(\omega_L t\right)|1,0\rangle_z$$
$$|\Psi_H\rangle\left(t\right) = |\Psi_H\rangle$$

For a measurement with the same readout laser pulse polarization ($|\chi\rangle_{ro} = |V\rangle$) as above, the probability of finding initial states $|\Psi_V\rangle/|\Psi_H\rangle$ after time t in the dark state are

$$P\left(|\Psi_D\rangle_V, t\right) = \|\langle\Psi_D|\ \Psi_V\rangle\left(t\right)\|^2 = \cos^2\left(\omega_L t\right) \tag{3.5}$$
$$P\left(|\Psi_D\rangle_H, t\right) = \|\langle\Psi_D|\ \Psi_H\rangle\left(t\right)\|^2 = 0.$$

This shows that states prepared in $|\Psi_H\rangle$ are not affected by magnetic fields in x-direction, whereas initial state $|\Psi_V\rangle$ experiences Larmor precession with period $T = \frac{\pi}{\omega_L}$. A time evolution of the atomic states with a field in x-direction can be found in Fig. 3.1.

Field in y-direction

For a field in y-direction, stating $b_y = 1$, $b_x = b_z = 0$ and $\phi = \frac{\pi}{2}$, the eigenvectors are

$$|\Phi_{+1}\rangle = \begin{pmatrix} \frac{-i}{2} \\ \frac{1}{\sqrt{2}} \\ \frac{i}{2} \end{pmatrix}, \qquad |\Phi_0\rangle = \begin{pmatrix} \frac{i}{\sqrt{2}} \\ 0 \\ \frac{i}{\sqrt{2}} \end{pmatrix}, \qquad |\Phi_{-1}\rangle = \begin{pmatrix} \frac{-i}{2} \\ \frac{-1}{\sqrt{2}} \\ \frac{i}{2} \end{pmatrix}.$$

(a) Larmor precession for magnetic field in z-direction.

(b) Larmor precession for magnetic field in x-direction.
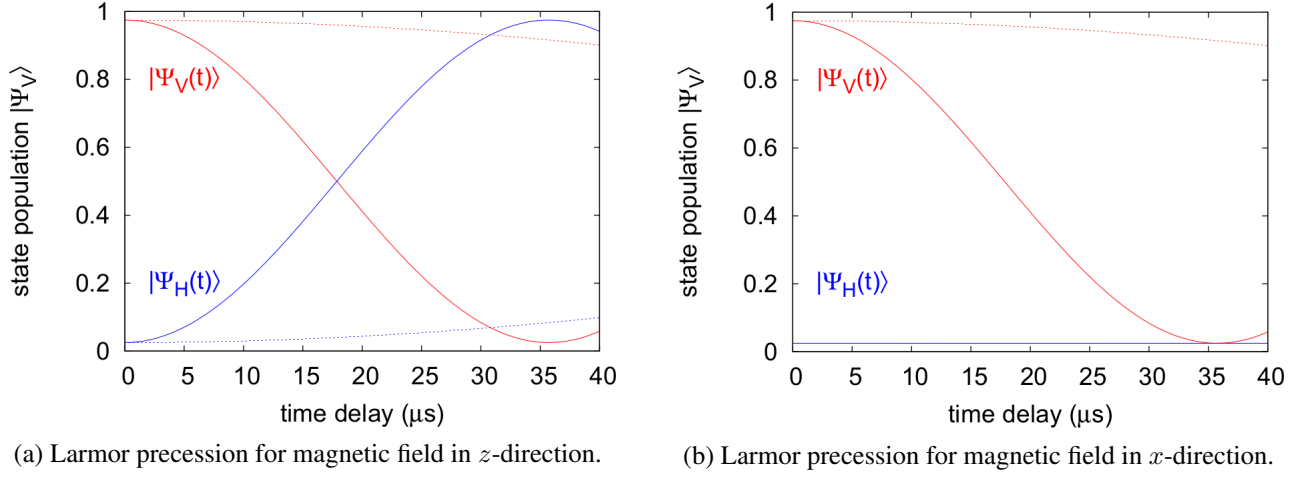
Figure 3.1.: Time evolutions for states $|\Psi_V\rangle$ and $|\Psi_H\rangle$. At a given delay t they are projected onto $|\Psi_V\rangle$. Solid lines show state evolution for 10 mG field , dashed lines show 1.6 mG field [7]

Expressing $|\Psi_V\rangle$ and $|\Psi_H\rangle$ in terms of $|\Phi_i\rangle$ yields

$$|\Psi_V\rangle = \frac{1}{\sqrt{2}}\left(|1,-1\rangle_z + |1,+1\rangle_z\right) \qquad\qquad = -i\,|\Phi_0\rangle$$

$$|\Psi_H\rangle = \frac{i}{\sqrt{2}}\left(|1,-1\rangle_z - |1,+1\rangle_z\right) \qquad = \frac{1}{\sqrt{2}}\left(|\Phi_{+1}\rangle + |\Phi_{-1}\rangle\right)$$

with a time evolution of

$$|\Psi_V\rangle\,(t) = |\Psi_V\rangle$$
$$|\Psi_H\rangle\,(t) = \cos\left(\omega_L t\right)|\Psi_H\rangle - i\sin\left(\omega_L t\right)|1,0\rangle_z\,.$$

If measuring these dynamics with a readout pulse polarization as above ($|\chi\rangle_{ro} = |V\rangle$), we will not observe any dynamics as

$$\langle\Psi_D|\,\Psi_V\rangle\,(t) = 1$$
$$\langle\Psi_D|\,\Psi_H\rangle\,(t) = 0.$$

Therefore we choose the readout pulse polarization to be $|\chi\rangle_{ro} = |H\rangle$ (i.e.$|\Psi_H\rangle = |\Psi_D\rangle$), which lets us observe similar dynamics as for a field in x-direction, just with the initial states being switched

$$P\left(|\Psi_D\rangle_V,t\right) = \|\langle\Psi_D|\,\Psi_V\rangle\,(t)\|^2 = 0$$
$$P\left(|\Psi_D\rangle_H,t\right) = \|\langle\Psi_D|\,\Psi_H\rangle\,(t)\|^2 = \cos^2\left(\omega_L t\right). \tag{3.6}$$

3.2. AC-Stark shift in an optical dipole trap

The AC-Stark shift is an effect that influences atoms exposed to strong oscillating electric fields (optical fields). From this effect arises a shift of the energies of the atom, which in our case is used for trapping a single atom in an optical dipole trap with one tightly focused beam, as described in sec. 2.3.1. This shift of the $5^2 S_{1/2}$, $F = 1$ ground state in energy can also be Zeeman state-dependent, if the polarization P of the dipole trap light has circular components in relation to the quantization axis [10] (for details to the other parameters of this equation, see (2.5))

$$\Delta E(\vec{x}) = \frac{\pi c^2 \Gamma}{2\omega_0^3} \cdot \left(\frac{2 + P g_F m_{F,z}}{\Delta_{2,F}} + \frac{1 - P g_F m_{F,z}}{\Delta_{1,F}} \right) \cdot I(\vec{x}) \tag{3.7}$$

The light of the dipole trap beam propagates along the z-axis, therefore the electric field is [26]

$$\vec{E}(\vec{x}) = \begin{pmatrix} E_x(\vec{x}) \\ E_y(\vec{x}) e^{i\delta} \\ 0 \end{pmatrix}$$

which leads to a polarization of

$$P = \frac{2 \left\| E_x(\vec{x}) \right\| \cdot \left\| E_y(\vec{x}) \right\| \sin(\delta)}{\left\| E_x(\vec{x}) \right\|^2 + \left\| E_y(\vec{x}) \right\|^2} \tag{3.8}$$

that is $P \in [-1, 1]$ for any general elliptical polarization, with special cases $P = 0$ for linear polarization and $P = \pm 1$ for σ^+ / σ^- circular polarization. For the coherence of the atomic state, only relative energy shifts between the Zeeman sub-states $|1, +1\rangle_z$, $|1, 0\rangle_z$ and $|1, -1\rangle_z$ are of interest. Following the calculations in [7], the shift that is state independent is

$$\Delta E_{all}(\vec{x}) = \frac{\pi c^2 \Gamma}{2\omega_0^3} \cdot \left(\frac{2}{\Delta_{2,F}} + \frac{1}{\Delta_{1,F}} \right) \cdot I(\vec{x}) \tag{3.9}$$

which corresponds to the trapping potential that all atoms see, independent of their specific Zeeman state and leads to no state evolution. For this reason, we define it to be the mean trapping potential $U_m(\vec{x}) := \Delta E_{all}(\vec{x})$. We get the relative energy shift by subtracting (3.9) from (3.7), which leaves a relative energy shift of the Zeeman states of

$$\Delta E_{rel}(\vec{x}) = \frac{\pi c^2 \Gamma}{2\omega_0^3} \cdot \left(\frac{1}{\Delta_{2,F}} - \frac{1}{\Delta_{1,F}} \right) P g_F m_{F,z} I(\vec{x})$$

causing an evolution of ground states of the atom. For more compact calculation, we define the the constant parameter R_{circ} to be

$$R_{circ} := \frac{\frac{1}{\Delta_{2,F}} - \frac{1}{\Delta_{1,F}}}{\frac{2}{\Delta_{2,F}} + \frac{1}{\Delta_{1,F}}} \tag{3.10}$$

now dividing the relative shift by the shift that all states experiences gives

$$\frac{\Delta E_{rel}(\vec{x})}{\Delta E_{all}(\vec{x})} = R_{circ} P g_F m_{F,z}.$$

Rearranging this gives

$$
\begin{aligned}
\Delta E_{rel}(\vec{x}) &= P \cdot R_{circ} g_F m_{F,z} \Delta E_{all}(\vec{x}) \\
&= P \cdot R_{circ} g_F m_{F,z} U_m(\vec{x})
\end{aligned}
\tag{3.11}
$$

which is similar to a shift of the atom's energy by the Zeeman effect with magnetic field in z-direction

$$\Delta E_{Zeeman} = \mu_B g_F m_{F,z} B_z.$$

For this reason, we can express the shift of the atom being in the ODT with circular polarization components in an external magnetic field in z-direction in a combined expression

$$
\begin{aligned}
\Delta E &= \Delta E_{Zeeman} + \Delta E_{rel}(\vec{x}) \\
&= \mu_B g_F m_{F,z} \left(B_z + \frac{1}{\mu_B} P \cdot R_{circ} \Delta U_m(\vec{x}) \right) \\
&= \mu_B g_F m_{F,z} B_{z,eff}(\vec{x})
\end{aligned}
\tag{3.12}
$$

that gives an effective field in z-direction $B_{z,eff}$ which includes the relative AC-Stark shift induced by the dipole trap laser beam and the external magnetic field. For calculating state evolutions, we can still follow the formalism of sec. 3.1, but instead of the magnetic field, we now use an effective magnetic field

$$\vec{B}_{eff}(\vec{x}) = \vec{B} + \frac{1}{\mu_B} P R_{circ} U_m(\vec{x}) \vec{e}_z. \tag{3.13}$$

Note that this effective magnetic field is now position dependent, due to the intensity profile of the dipole trap beam, whereas we assume the external magnetic field $\vec{B}$ to be spatially constant within the volume of the dipole trap.

For an optimal state coherence, we want completely linearly polarized light to interact with the atom ($\vec{B}_{eff}(\vec{x}) = \vec{B}$). Therefore a polarizer is installed between the coupler of the dipole trap light and the dichroic mirror that sends the dipole trap light to the objective (see Fig. 2.3). The angle of the polarizer unfortunately can not be set a priori due to birefringence of the optical components (mainly the glass cell) in the beam path between polarizer and atom. The birefringence is temperature dependent, which makes a temperature stabilization of the experimental setup necessary [24].

To distinguish between elliptical polarization of the ODT light and real magnetic fields in a measurement, we change the trap depth/intensity of the dipole trap beam, which will also change the effective magnetic field according to (3.13). The change we observe between measurements with different dipole trap beam intensities can then be attributed to elliptical polarization of the dipole trap light only. By changing the trap depth and analyzing state evolutions, we therefore can determine the angle of the polarizer experimentally. A scheme on how to do this can be found in [7].

3.3. Effects of strong focusing and oscillation of the atom in the trap

As of now, the effect of elliptical polarization of the dipole trap beam on the atomic state was analyzed and the effect can be minimized by linear polarization of the optical dipole trap (ODT) beam. But there will be additional local elliptical polarization in the focal region, due to the focusing of the ODT beam [29, 35, 42, 27]. This leads to energy shifts of the atomic Zeeman states resulting in time evolution of the atomic state. This effect is depending strongly on the position of the atom in the trap. When measuring many atoms subsequently, this will lead to decoherence, as the starting conditions for the motion of the atom in the trap are thermally distributed.

3.3.1. Focusing a linearly polarized Gaussian beam

The incident beam of the optical dipole trap is a Gaussian beam that is then focused by the microscope objective. This objective focuses the beam so tightly (high numerical aperture (NA)) that the paraxial approximation of Gaussian ray optics does no longer hold. Therefore deviations from the Gaussian beam arise, especially in the vicinity of the focus of the beam. For a linearly polarized beam the field vector will have longitudinal components close to the focal point. This effect was first described for the focus of a plane wave by a lens in [42, 27]. With additions for Gaussian optics it can also be applied to our case [29]. For a Gaussian beam propagating along the z-axis with incidental polarization along the x-axis, will have a polarization component perpendicular to the optical axis and a longitudinal polarization component parallel to the optical axis in the focal area. Due to the symmetry of the problem, we choose cylindrical coordinates (r, ϕ, z), where the origin is the focal point and the angle ϕ is chosen with respect to the x-axis. The components of the electrical field vector $\vec{E}$ in the vicinity of the focal point are given by

$$
\vec{E}\left(r, z\right) = \left(\begin{array}{c} E_x\left(r, z\right) \\ E_y\left(r, z\right) \\ E_z\left(r, z\right) \end{array} \right) = E_o \left(\begin{array}{c} F_0\left(r, z\right) + F_2\left(r, z\right)\cos\left(2\phi\right) \\ F_2\left(r, z\right)\sin\left(2\phi\right) \\ 2iF_1\left(r, z\right)\cos\left(\phi\right) \end{array} \right)
$$

where E_0 is a scaling constant and $F_i\left(r, z\right)$ are the diffraction integrals calculated as

$$
F_0\left(r, z\right) = \int_0^\alpha d\theta \, \exp\left(\frac{-f^2 \tan\left(\theta\right)^2}{w^2} \right) \sqrt{\cos\left(\theta\right)} \left(1 + \cos\left(\theta\right)\right) J_0\left(kr\sin\left(\theta\right)\right) e^{ikz\cos(\theta)} \sin\left(\theta\right)
$$

$$
F_1\left(r, z\right) = \int_0^\alpha d\theta \, \exp\left(\frac{-f^2 \tan\left(\theta\right)^2}{w^2} \right) \sqrt{\cos\left(\theta\right)} \sin\left(\theta\right) J_1\left(kr\sin\left(\theta\right)\right) e^{ikz\cos(\theta)} \sin\left(\theta\right)
$$

$$
F_2\left(r, z\right) = \int_0^\alpha d\theta \, \exp\left(\frac{-f^2 \tan\left(\theta\right)^2}{w^2} \right) \sqrt{\cos\left(\theta\right)} \left(1 - \cos\left(\theta\right)\right) J_2\left(kr\sin\left(\theta\right)\right) e^{ikz\cos(\theta)} \sin\left(\theta\right).
$$

Here J_0, J_1, J_2 are Bessel-J functions of the first kind, f is the focal length of the objective, w is the radius of the Gaussian beam entering the microscope objective. These integrals sum partial waves coming from infinitesimal rings of the objective at an angle θ relative to the z-axis up to the angle α given by the NA of the objective. As these integrals have to be solved a lot of times in order to get a map of the electrical field in the focal area, they can be approximated as [29]

$$F_0\left(r,z\right) \approx F_0\left(0,0\right) \frac{1}{\sqrt{1+\frac{z^2}{z_R^2}}} \exp\left(-\frac{r^2}{w_0^2\left(1+\frac{z^2}{z_R^2}\right)}\right)$$

$$F_1\left(r,z\right) \approx F_0\left(0,0\right) \frac{1}{2z_R} \frac{r}{1+\frac{z^2}{z_R^2}} \exp\left(-\frac{r^2}{w_0^2\left(1+\frac{z^2}{z_R^2}\right)}\right)$$

$$F_2\left(r,z\right) \approx F_0\left(0,0\right) \frac{1}{\left(2z_R\right)^2} \frac{r^2}{\left(1+\frac{z^2}{z_R^2}\right)^2} \exp\left(-\frac{r^2}{w_0^2\left(1+\frac{z^2}{z_R^2}\right)}\right)$$

where $w_0 = \frac{\lambda f}{\pi w}$ the beam waist at the focus and $z_R = \frac{\pi w_0}{\lambda}$ the Rayleigh length from Gaussian ray optics. The value of $F_0\left(0,0\right)$ then is

$$F_0\left(0,0\right) = \int_0^\alpha d\theta \, \exp\left(\frac{-f^2\tan\left(\theta\right)^2}{w^2}\right) \sqrt{\cos\left(\theta\right)}\left(1+\cos\left(\theta\right)\right)\sin\left(\theta\right).$$

These formulas allow us to calculate the electrical field in the focal area, which is done by Mathematica for an initial polarization along the x-axis. E_x and E_z are plotted in Fig. 3.2, while there are no noteworthy contributions of E_y. Note that for the transversal component E_x, the distribution around the focus is similar to the distribution expected by Gaussian optics. The longitudinal component E_z is approximately one order of magnitude smaller than the transversal component and maximal at a certain distance from the focal spot along the x-axis. In Fig. 3.2 it is obvious that the longitudinal component E_z has a sign-change when crossing the y-z-plane. Combining both field components, the polarization of the light is slightly elliptical rotating clockwise/anticlockwise depending on the sign of x. As described in the previous section, elliptically polarized light shifts the Zeeman state relative to each other in energy due to the state-dependent and position-dependent AC-Stark effect, which leads to dephasing of the atomic states. If we look at a measurement of many atoms this leads to decoherence, as the initial position and motion of the atom in the trap are not the same for all atoms, but instead obey a thermal distribution.

3.3.2. Time evolution of atomic states in the ODT field

For calculating the atomic state evolution due to the polarization effects of strong focusing, we can use the same formalism as in sec. 3.2. But some adjustments have to be performed, as the

(a)

(b)

(c)

(d)
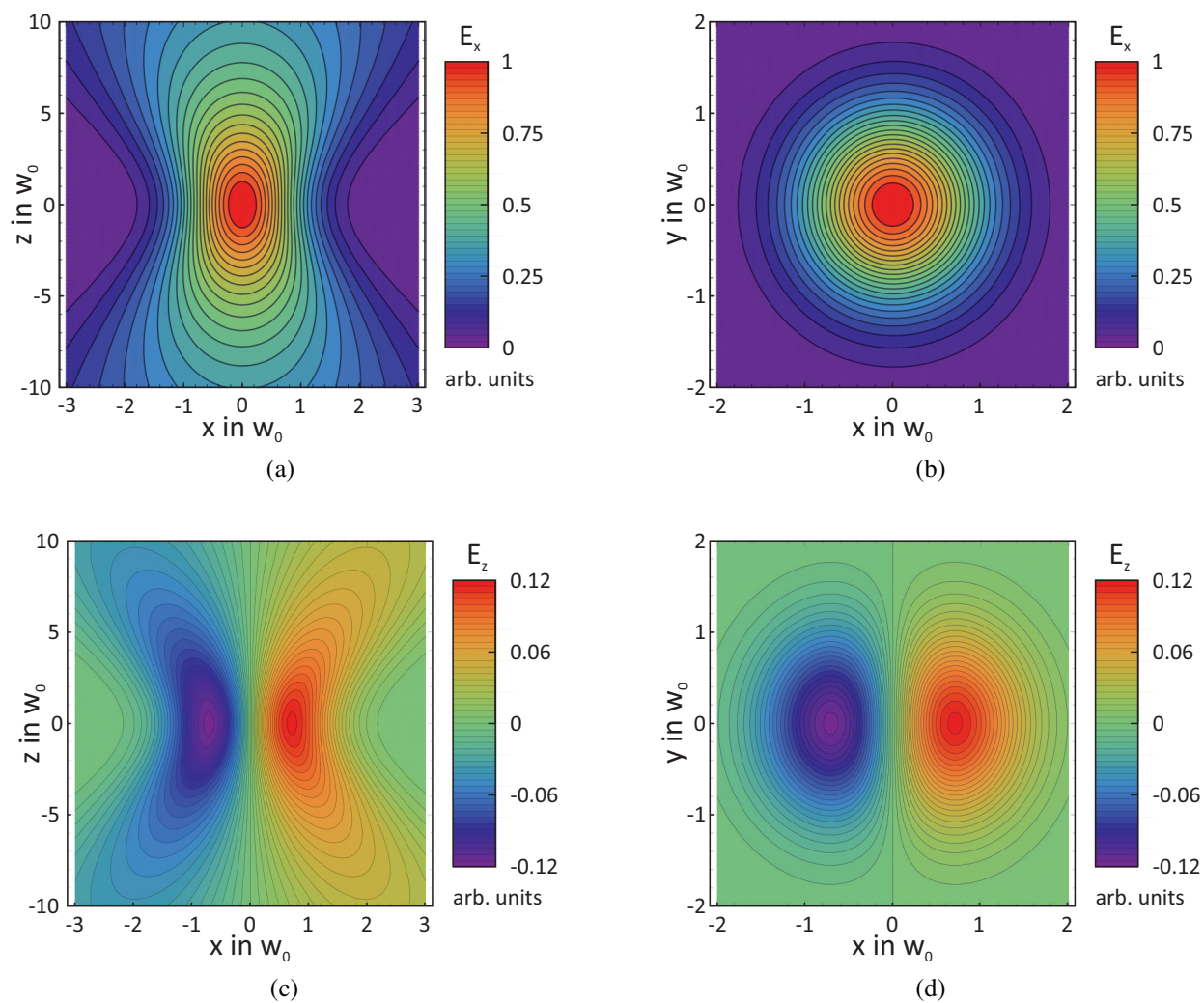
Figure 3.2.: Electrical field profiles in focal region (a)+(b): E_x transversal component; (c)+(d): E_z longitudinal component, note the sign change along x-axis. [26]

electrical field now is

$$\vec{E}\left(\vec{x}\right) = \begin{pmatrix} E_x\left(\vec{x}\right) \\ 0 \\ E_z\left(\vec{x}\right) \end{pmatrix}$$

which leads to a polarization P of

$$P\left(\vec{x}\right) = sgn\left(x\right) \sqrt{1 - \left(\frac{\left|E_x\left(\vec{x}\right)\right|^2 - \left|E_z\left(\vec{x}\right)\right|^2}{\left|E_x\left(\vec{x}\right)\right|^2 + \left|E_z\left(\vec{x}\right)\right|^2}\right)^2}$$

where $sgn\left(x\right)$ is the sign of the x-component of the position vector $\vec{x}$. Whilst continuing to use R_{circ} as defined in (3.10) and $U_m\left(\vec{x}\right)$ as defined in (3.11), we can write the relative state shift as

$$\Delta E_{rel}(\vec{x}) = P\left(\vec{x}\right) R_{circ} g_F m_{F,y} U_m\left(\vec{x}\right).$$

Note that we have to use $m_{F,y}$ here compared to $m_{F,z}$ in (3.11), as the system here is in eigenstates to the $\hat{F}_y$ angular momentum operator [29]. Therefore this effect resembles a magnetic field in y-direction with

$$B_{long}\left(\vec{x}\right) = \frac{R_{circ}}{\mu_B} P\left(\vec{x}\right) U_m\left(\vec{x}\right)$$

and

$$\vec{B}_{eff}(\vec{x}) = \vec{B} + B_{long}\left(\vec{x}\right) \vec{e}_y. \tag{3.14}$$

As this effect is strongly position dependent ($B_{long}(\vec{0}) = 0$, $\max(B_{long})$ at $x \approx 0.9w_0$) and the motion of an atom in the trap, every atom will pass areas of high field strength, while moving in the trap. For the reason that the atoms' initial conditions, to be precise, the position and the velocity an atom has when it sends out a photon, are thermally distributed, every single atom will have an individual state evolution. When compared to the state evolution for a magnetic field in y-direction, as given in sec. 3.1.1, one can see that the prepared atomic state $|\Psi_H\rangle = \frac{i}{\sqrt{2}}\left(|1,-1\rangle_z - |1,+1\rangle_z\right)$ will undergo Larmor precession, while the state $|\Psi_V\rangle = \frac{1}{\sqrt{2}}\left(|1,-1\rangle_z + |1,+1\rangle_z\right)$ remains unaffected. This effect cannot be compensated for, the reason being that the state evolution of every atom is different and initial conditions of the atom are individual and unknown. For a measurement averaged over many individual atomic state evolutions, this results in a quickly decaying coherence for $|\Psi_H\rangle$, while $|\Psi_V\rangle$ will stay coherent. An additional feature is that the effective magnetic field is antisymmetric to the z-axis. If we now consider atomic motion in the x-y-plane only, this motion is symmetric with respect to the z-axis. Therefore, a phase acquired by the atomic state on one side of the z-axis during the first half of its motional period, will be withdrawn during the second half of its motional period on the other side of the z-axis, where the atom will acquire the same phase, but with the opposite sign.
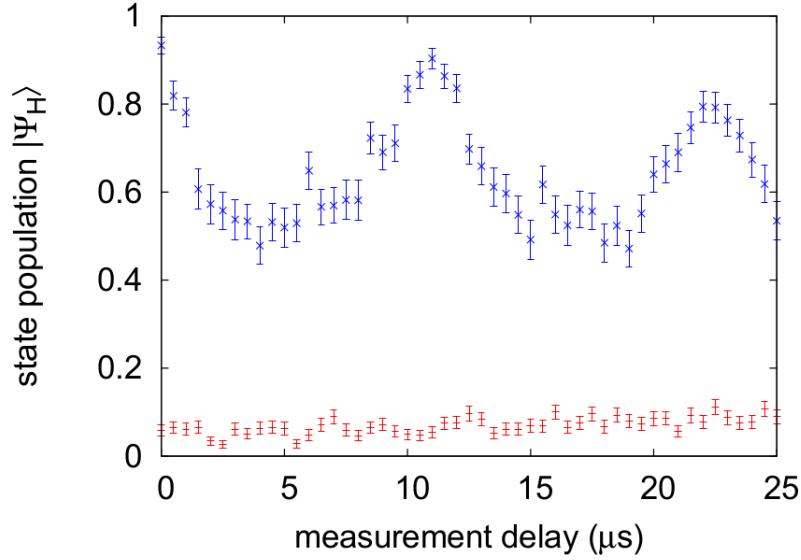
Figure 3.3.: Measured time evolution of the atomic states, while moving in the effective magnetic field B_{long} along the y-direction created by the polarization effects of the ODT. At a delay time t after photon emission, the atomic state is projected onto $|\Psi_H\rangle$. The initially prepared atomic state $|\Psi_H\rangle$ (blue) dephases and rephases after one radial oscillation in the trap, while $|\Psi_V\rangle$ (red) is unaffected. [7]

Assuming a motion of the atom in the x-y-plane only is reasonable for short evolution times, as the trapping frequency in the x-y-plane (radial trapping) is

$$\Omega_r = \sqrt{\frac{2\pi z_R}{\lambda}} \cdot \Omega_z \approx 10.01 \cdot \Omega_z$$

much higher than the trapping along the z-axis for our experimental parameters ($\lambda = 852$ nm, $z_R = 13.59$ μm). This results in a rephasing of all $|\Psi_H\rangle$ atomic states after one complete oscillation in radial direction, which means that $|\Psi_H\rangle$ will be coherent again after one oscillation in radial direction for a measurement averaged over many atomic state evolutions. This behavior can be seen in Fig. 3.3.

4. Compensation of external magnetic fields

This chapter will follow up on the effects described in the previous chapter, as they have to be compensated in order to achieve high visibilities for atom-atom entanglement experiments over long distances. Fig. 2.9 gives an overview of the timing in atom-atom entanglement experiments performed over a distance of 400 m. As shown there, the delay time between photon emission by the atom and atomic state readout is on the order of 10 µs. Within that delay time, the contrast of atom-photon correlation should not reduce by more than 1.0% [7], which was crucial for the test of Bell's inequality [30]. In general, the visibility V of atom-atom entanglement including all effects should be well above $V > \frac{2}{2\sqrt{2}} \approx 0.707$ in oder to violate Bell's inequality. When going to longer distances, as planned for the future, the delay time will increase and so will the requirements for atomic state coherence. We set ourselves the goal to limit the allowed ambient magnetic field to less than 1 mG for each trap. Sources that create magnetic field fluctuations are plentiful. Sources worth mentioning is the underground line passing by the laboratory at a distance of 60 m, as well as all devices containing magnetic parts and electronic components used in the lab, especially the ion getter pump and power converters. These sources create an ambient magnetic field $\vec{B}_a$ that fluctuates on all timescales relevant for the experiment. This chapter will give an insight into the setup and the procedure how to compensate this ambient magnetic field.

4.1. Active magnetic field stabilization

In our experiment an active stabilization of the magnetic fields is used, meaning that we try to generate a magnetic field $\vec{B}_{comp}$, that compensates the ambient magnetic field at the position of the atom at all times

$$\vec{B}_{comp}\left(\vec{x}_{at}, t\right) = -\vec{B}_a\left(\vec{x}_{at}, t\right).$$

For this task one needs an active feedback loop, able to generate and control $\vec{B}_{comp}$. It consists of a magneto-resistive feedback sensor[1], a PID-controller, a triple current source and three pairs of compensation coils. The sensor monitors the magnetic field for all three spatial directions

---

[1]Honeywell HMC 1053
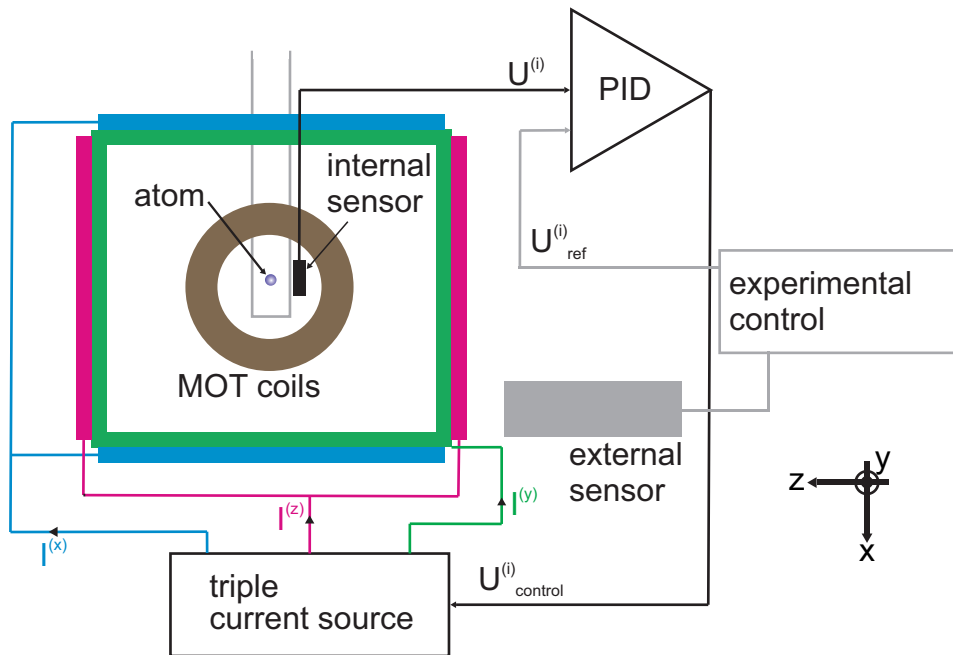
Figure 4.1.: Schematic drawing of the magnetic field compensation setup, with a pair of rectangular coils in Helmholtz configuration for each spatial direction to generate $\vec{B}_{comp} = -\vec{B}_a$, compensating the ambient magnetic field. The internal sensor output is compared to a reference, the current sent to the compensation coils is controlled accordingly. Note that the internal magneto-resistive sensor is placed inside the MOT coils, therefore it needs to be calibrated with respect to the more stable external senor and $U_{ref}^{(i)}$ needs to be adjusted every few minutes which is performed automatically by the experimental control software. Further implications of this are described in sec. 4.3.
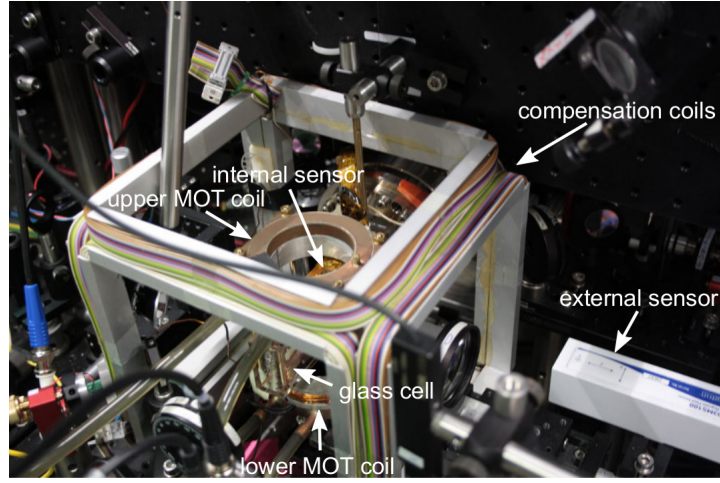
Figure 4.2.: Experimental setup of the magnetic field compensation in lab 2. The atom is trapped inside the vacuum glass cell, the internal sensor is located close to the glass cell wall. The trap and the internal senor are both surrounded by the MOT coils. The compensation coils enclose the whole arrangement, in order to generate a homogeneous field at the location of the atom. The external sensor is placed outside of the compensation coils. [7]

(x, y, z) and generates a voltage signal for each spatial direction $i \in \{x, y, z\}$ that depends linearly on the magnetic field

$$U^{(i)} = s^{(i)} \cdot B^{(i)} + U_{offset}^{(i)} \tag{4.1}$$

with an offset voltage of $U_{offset}^{(i)}$ and a sensitivity $s^{(i)}$ which differs slightly for each spatial direction, but is on the order of $1 \frac{mV}{mG}$ after a preamplifier. The measured sensitivities can be found in [7]. This signal is sent to a PID-Controller that compares the signal to a predefined reference voltage $U_{ref}^{(i)}$. The response of the PID to a difference between signal and reference is continuously calculated in optimized fashion taking proportional, integral and derivative terms into account, hence its name. The response of the PID then adjusts control voltages $U_{control}^{(i)}$ for each spatial direction for a triple current source that generates the currents needed for compensation. For every spatial direction the current goes to a pair of rectangular coils operated approximately in Helmholtz configuration and placed around the vacuum glass cell where the atomic trap is located. The coils then generate a field such that $U^{(i)} = U_{ref}^{(i)}$.

A schematic drawing of the setup and a picture of the real setup are presented in Fig. 4.1 and Fig. 4.2. These components form a feedback loop that is able to compensate a varying magnetic field with fluctuations up to ~ 200 Hz [29]. There are several limitations to this scheme, that will be discussed in the following sections.

4.2. High frequency magnetic field fluctuations

As the speed of the feedback loop is limited to ~ 200 Hz by the time constant of the integrator of the PID in the feedback loop [29], all fluctuations with components at higher frequencies will not be compensated. Every magnetic field fluctuation will influence the atomic state. Of special interest for the experiment are those fluctuations, that happen on the same timescale as the experiments ($\sim 1 - 100$ μs) and therefore will not average out over the time evolution of a prepared atomic state. To estimate those fluctuations, the signals $U^{(i)}(t)$ of the feedback sensor was measured with an oscilloscope at a temporal resolution of 40 μs, while the feedback loop was active. This measured trace of sensor signal can be transformed into a trace of fluctuating field magnetic field using (4.1). To analyze the deviations from the average field

$$\Delta B^{(i)}(t) = B^{(i)}(t) - \overline{B^{(i)}}$$

with $\overline{B^{(i)}}$ the average of all measurements for each spatial direction, they were summed up in normalized histograms (e.g. for the setup in lab 1 in Fig. 4.3). Shown there is also a fit of the histograms to a normal distribution

$$\varrho_{HF}^{(i)}\left(\Delta B^{(i)}\right) = \frac{1}{\sqrt{2\pi \left(\sigma_{HF}^{(i)}\right)^2}} \exp\left(-\frac{\left(\Delta B^{(i)} - \mu\right)^2}{2\left(\sigma_{HF}^{(i)}\right)^2}\right) \tag{4.2}$$

where μ is the asymmetry of the fluctuations and $\sigma_{HF}^{(i)}$ is the standard deviation of the high-frequency magnetic field fluctuations. The results for both labs are written down in table 4.1. The asymmetry μ turned out to be negligible. A numerical Fourier analysis of the trace of fluctuations revealed, that there are small contributions for almost all frequencies, with larger contributions of the higher harmonics of the power-line frequency (50 Hz).

4.3. Stability of the magnetic feedback sensor

Another limitation to the performance for short-term ('shot-to-shot') stability and long-term stability (hours timescale) of the magnetic field compensation is the type of magnetic field sensor used for the feedback loop and its position inside the volume enclosed by the MOT coils (see Fig 4.1 and 4.2). The feedback sensor is a three-axis sensor, for each spatial direction there is a Wheatstone bridge with embedded magneto-resistive elements. These cause a voltage imbalance at the bridge, if a magnetic field is applied. After amplification of the initial signal, sensitivities on the order of $1\frac{mV}{mG}$ are achieved. Advantages of this sensor are its compact design, allowing for placement close to the atomic trap, its high sensitivity and its high rate of measurements. The major disadvantage is that the magneto resistive elements in the sensor need a certain magnetic polarization for their function. This magnetization can be changed by applying strong magnetic

(a) Field fluctuations in x-direction.

(b) Field fluctuations in y-direction.

(c) Field fluctuations in z-direction.
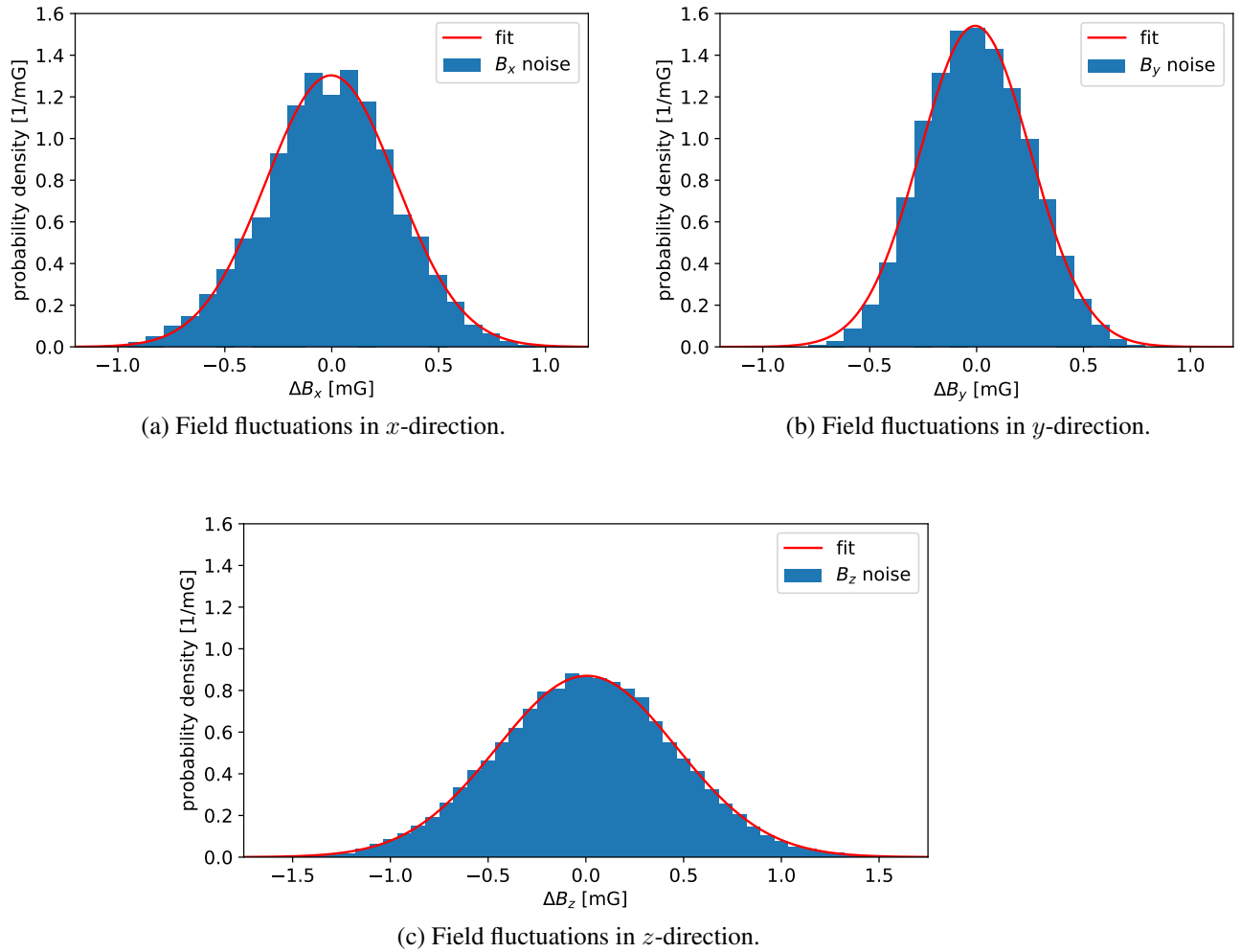
Figure 4.3.: Remaining magnetic field fluctuations up to $f \leq 12.5$ kHz with active magnetic field stabilization in lab 1. Displayed is the probability density in $\left[\frac{1}{mG}\right]$ for magnetic field fluctuations in respective spatial directions. The fit is done according to a normal distribution as given in (4.2).

fields. Such high fields are created by the MOT coils, when they are switched on for loading an atom into the trap (see sec.2.3). The feedback sensor is then exposed to fields of 26.25 G (lab 1) and 40.92 G (lab 2) [7] respectively, which clearly saturate the sensor and change its magnetization. Therefore a sensor reset is set up, consisting of two current pulses in opposite directions sent through coil straps, that are directly integrated into the sensor, in order to restore the original magnetization of the sensitive areas [29]. This sensor reset is performed every time after an atom is loaded into the trap and it is not perfect, i.e. that $U_{offset}^{(i)}$ from (4.1) can change slightly after a reset. For that reason the magnetic field that the feedback loop stabilizes on for the subsequent event of atom-photon entanglement changes by

$$\Delta B_{SR}^{(i)} = \frac{\Delta U_{offset}^{(i)}}{s^{(i)}}.$$

These so called sensor reset jumps were experimentally recorded and quantified by a measurement where the value of the feedback sensor was compared to an additional external sensor[2] (see Fig. 4.1 and Fig. 4.2), that is positioned outside of the MOT coils and compensation coils and is used as a stable reference. The external sensor is a fluxgate-type sensor with a certified, long-term stable sensitivity of $10\frac{mV}{mG}$, but it is to big to be positioned close to the atom inside of the current compensation coils, as necessary for the feedback loop. For measuring $\Delta B_{SR}^{(i)}$, the two sensors were initially compared, then the MOT coils were switched on for several seconds. After switching off the MOT coils and resetting the internal sensor as described above, the two sensors were compared again. When now comparing the difference between both sensors before and after MOT on/off switching and sensor reset, the remaining difference is the sensor reset jump

$$\Delta B_{SR}^{(i)} = \left(B_{int,before}^{(i)} - B_{ext,before}^{(i)} \right) - \left(B_{int,after}^{(i)} - B_{ext,after}^{(i)} \right).$$

To quantify these reset jumps, about 2000 reset cycles were recorded and summed up in normalized histograms (see Fig. 4.4). They were fitted to a normal distribution

$$\varrho_{SR}^{(i)} \left(\Delta B_{SR}^{(i)} \right) = \frac{1}{\sqrt{2\pi \left(\sigma_{SR}^{(i)} \right)^2}} \exp\left(-\frac{\left(\Delta B_{SR}^{(i)} - \mu \right)^2}{2 \left(\sigma_{SR}^{(i)} \right)^2} \right) \tag{4.3}$$

where $\sigma_{SR}^{(i)}$ is the standard deviation of the distribution (results for both labs see table 4.1) and μ is the average value of the sensor reset jumps. As $\mu \neq 0$ for this measurement, this indicates that the sensor reset jumps do not only change the magnetic field shot-to-shot, but they also induce a drift of the feedback sensor. Given that the drifts are on the order of 1 to 5 mG per hour [7], they have to be compensated as well. As the external fluxgate sensor is much more stable, it is used to calibrate the feedback sensor every few minutes.

---

[2]Bartington Mag-03MS100

(a) Sensor jumps in x-direction.

(b) Sensor jumps in y-direction.

(c) Sensor jumps in z-direction.
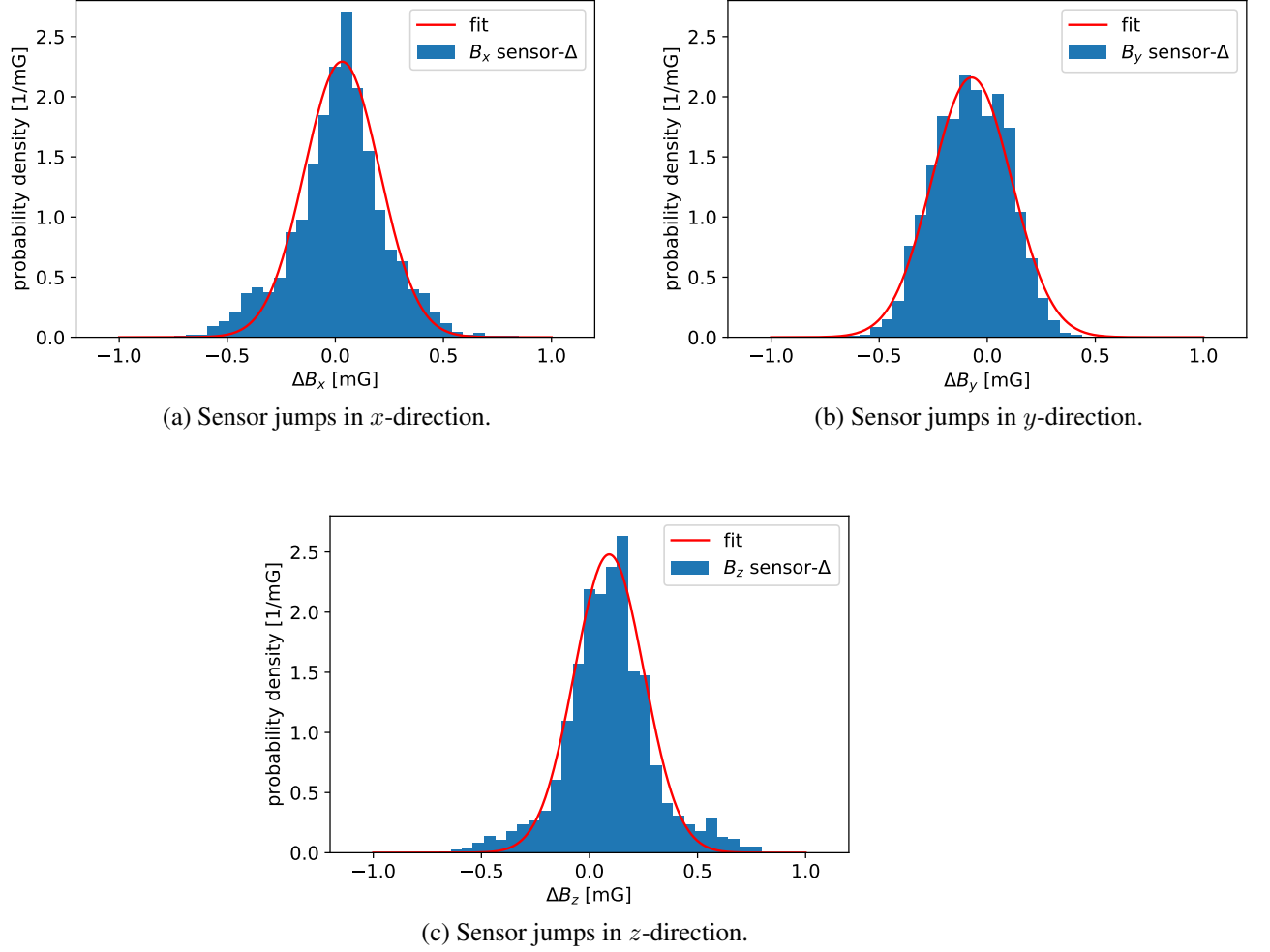
Figure 4.4.: Sensor reset jumps after MOT on/off switching and sensor reset in lab 2. These jumps occur every time after a new atom is loaded into the trap (i.e. the MOT coils were switched on) and the sensor is subsequently reset.

lab 1	$\sigma_{HF}^{(i)}$ [mG]	$\sigma_{SR}^{(i)}$ [mG]	$\sigma_{IH}^{(i)}$ [mG]	lab 2	$\sigma_{HF}^{(i)}$ [mG]	$\sigma_{SR}^{(i)}$ [mG]
x	0.31	0.80	0.02	x	0.63	0.17
y	0.26	0.25	0.19	y	0.30	0.18
z	0.46	0.20	0.08	z	0.55	0.16

Table 4.1.: Magnetic field fluctuations at the 'shot-to shot' timescale. $\sigma_{HF}^{(i)}$ and $\sigma_{SR}^{(i)}$ are the standard deviations of the normal distributions as given in (4.2) and (4.3). The effect of the inhomogeneity of the compensation field is characterized by $\sigma_{IH}^{(i)}$ from (4.4).

4.4. Inhomogeneity of the compensation field

Another limitation to the achievable stability of magnetic fields for the atom is, that it is impossible to measure the magnetic field directly at the position of the atom. Therefore an additional requirement for the feedback loop to work well is, that the ambient magnetic field is the same at the position of the atom and the position of the feedback sensor

$$\vec{B}_a\left(\vec{x}_{at}, t\right) \stackrel{!}{=} \vec{B}_a\left(\vec{x}_{sens}, t\right)$$

As [29] states, gradients of the ambient field can be neglected, as the distance between the atom and the feedback sensor (25 mm) is small, compared to all sources of fluctuating magnetic fields (e.g. power converters of lab electronics). Sources that have a constant magnetic field, such as the ion-getter pump, do not limit the stability, as they can be compensated for by initial calibration. Another requirement is, that the compensation field should also be homogeneous

$$\vec{B}_{comp}\left(\vec{x}_{at}, t\right) \stackrel{!}{=} \vec{B}_{comp}\left(\vec{x}_{sens}, t\right).$$

Here the geometry of the compensation coils is critical. For the compensation coils used in the experiment (e.g. in lab 1: inner diameter $l_x = 19$ cm, $l_y = 22$ cm, $l_z = 22$ cm with windings $N_x = 203$, $N_y = N_z = 250$), the field shows small gradients between the position of the atom (origin, $\vec{x}_{at} = \vec{0}$) and the position of the sensor (lab 1: $\vec{x}_{sens} = (-1,\ 18.5,\ -14)$ mm). If we now assume, that the magnetic field is compensated perfectly at the position of the feedback sensor (within the bandwidth of the compensation loop$\sim$ 200 Hz), we can estimate what the residual magnetic field fluctuations at the position of the atom are. Therefore a trace of magnetic field fluctuations was recorded, while the compensation was switched off. Then with the help of the Biot-Savart law, we could numerically calculate which currents $\vec{I}_{comp}$ would be sent through the compensation coils to compensate the ambient field such that

$$\vec{B}_a\left(\vec{x}_{at}, t\right) = -\vec{B}_{comp}\left(\vec{x}_{sens}, t\right).$$

Then a simulation of the compensation coil setup yields the field at the position of the atom for $\vec{I}_{comp}$. The residual fluctuations due to inhomogeneity of the compensation field then are

$$\Delta B_{IH}^{(i)} = \vec{B}_a\left(\vec{x}_{at}, t\right) - \vec{B}_{comp}\left(\vec{I}_{comp}, \vec{x}_{at}, t\right).$$

These fluctuations are shown in Fig. 4.5 for lab 1 as a normalized histogram. Additional fits to a normal distribution

$$\varrho_{IH}^{(i)}\left(\Delta B_{IH}^{(i)}\right) = \frac{1}{\sqrt{2\pi\left(\sigma_{IH}^{(i)}\right)^2}} \exp\left(-\frac{\left(\Delta B_{IH}^{(i)} - \mu\right)^2}{2\left(\sigma_{IH}^{(i)}\right)^2}\right) \tag{4.4}$$

quantify these fluctuations, with results given in table 4.1. This effect is small compared to those described in sec. 4.2 and 4.3.

(a) Residual field fluctuations in x-direction.

(b) Residual field fluctuations in y-direction.

(c) Residual field fluctuations in z-direction.
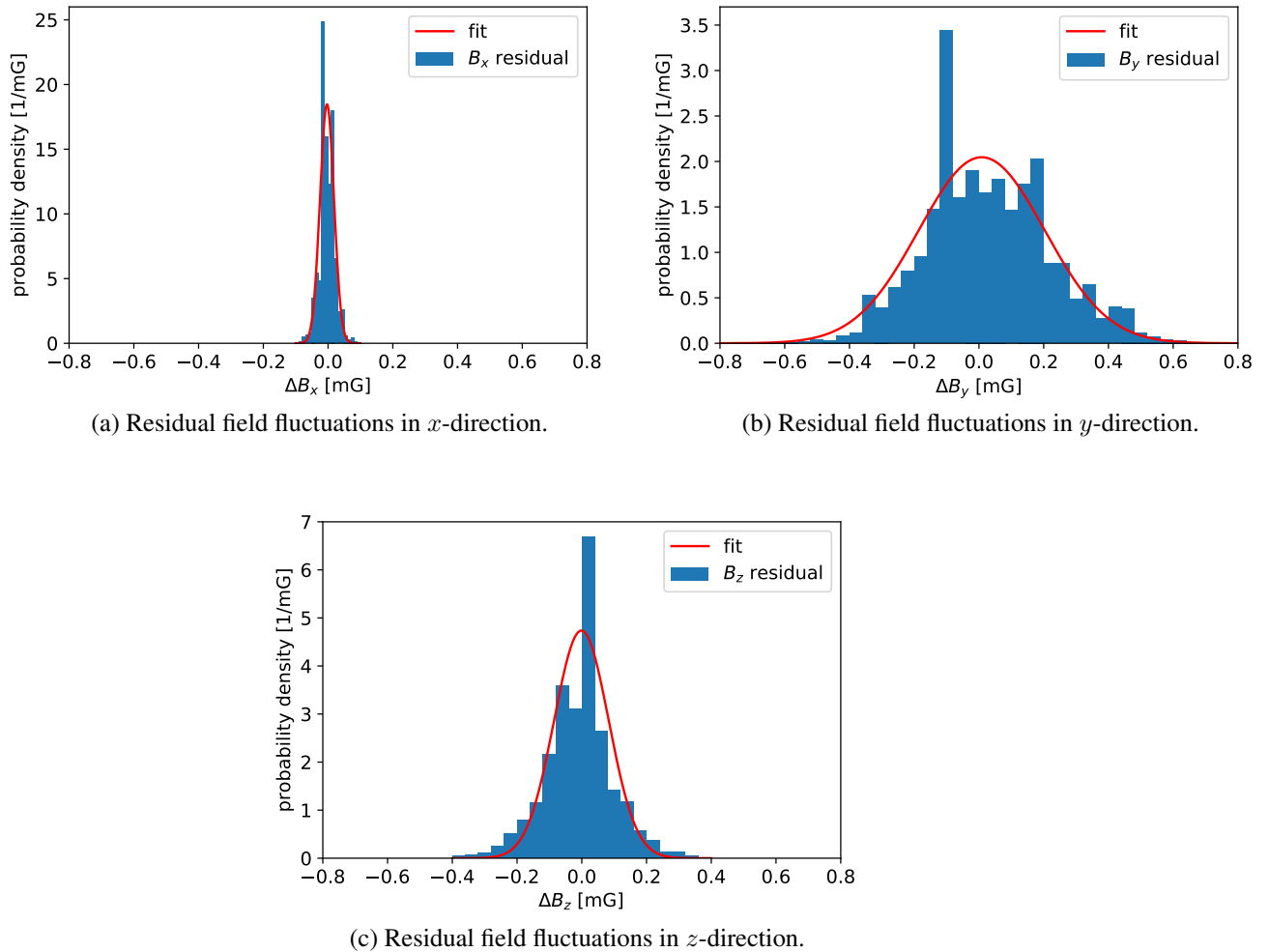
Figure 4.5.: Residual field fluctuations at the position of the atom due to inhomogeneities of the compensation field. Note that the fluctuations along the x-direction are much smaller compared to the other directions, because the feedback sensor is very close to the atom in x-direction.

4.5. Summary

This chapter described how ambient magnetic fields causing a time evolution of the prepared atomic states are compensated. The compensation can also compensate for initial elliptical polarization of the ODT leading to a effective magnetic field on the atom as described in sec. 3.2. The active magnetic field stabilization can compensate static and fluctuating fields within its feedback bandwidth. Its limitations are the long-term stability, as the internal sensor drifts when exposed to strong magnetic fields. To counteract that drift the internal sensor is calibrated with respect to a stable external sensor every few minutes. Furthermore, magnetic fields will fluctuate for every single realization of a atomic state evolution due to field fluctuations that are outside of the bandwidth of the feedback loop, imperfect internal sensor resets after loading an atom and inhomogeneities of the compensation field between internal sensor and the atom trap. In table 4.1 we can see that the 'shot-to-shot' fluctuations due to inhomogeneities of the compensation field are smaller than those of the other effects.

Outlook

This analysis allows to think of an improvement of the 'shot-to-shot' stability of magnetic fields by replacing the small magneto-resistive sensor used for the feedback loop. As the effect of inhomogeneities of the compensation is small compared to other effects influencing the 'shot-to-shot' stability, it allows for larger distances between the position of the atom trap and the feedback sensor used for the compensation loop. When additionally implementing a revision of the compensation coils such that they enclose the whole experimental housing, the gradients of the compensation field are further reduced. Simulations showed that the distance between atom trap and feedback sensor can then be increased to $d \approx 25\,\mathrm{cm}$ (compared to $d = 2.5\,\mathrm{cm}$ at the moment) while maintaining the same level of fluctuations due to inhomogeneities of the compensation field as there are right now. This allows for the use of the more stable but larger fluxgate-type sensor instead of the magneto-resistive sensor as the feedback sensor for magnetic field compensation. That would eliminate the shot-to-shot' fluctuations due to the imperfect reset of the magneto resistive sensor described in sec. 4.3 and drifts of the magneto-resistive sensor itself.

5. Analysis of measured atomic state evolution using numerical simulations

In this chapter I describe a way how to gauge the active magnetic field compensation system that was described in Chapter 4. For optimal coherence of the atomic state, the effective magnetic field affecting the atom should be $\vec{B}_{eff}(\vec{x}_{at}) = \vec{0}$, where $\vec{B}_{eff}(\vec{x})$ is defined as in (3.13) and $\vec{B}_{eff}(\vec{x})$ is composed of the actual magnetic field and the Zeeman state dependent AC-Stark shift. To achieve optimal state coherence, we can unfortunately not use a strong magnetic guiding field for this specific experiment, as a strong guiding field along the z-direction does not work [7], whereas a strong guiding field along the y-direction could create state coherence up to a few ms for some state[29], with the trade-off, that the prepared atomic state mixes with other states very rapidly reducing the visibility of atom-atom entangled states to around 70%[29], which is not sufficient to violate Bell's inequality in this experiment.

The experimental challenge is to find a set reference voltages $U_{ref}^{(i)}$ of the active magnetic feedback loop (see Fig. 4.1), such that the loop stabilizes the magnetic field (within its limitations) to $\vec{B}_{eff}(\vec{x}_{at}) = \vec{0}$. To determine $\vec{B}_{eff}(\vec{x}_{at})$ the most direct and only possible way is to experimentally measure the evolution of atomic states by reading out the state population after a time delay. Such measurements are time consuming (on the order of 2 hours) as each measurement is performed on a single atom and has to be repeated many times . Such a measurement has to be performed up to twice a day, as parameters influencing $\vec{B}_{eff}(\vec{x}_{at})$ are:

- Temperature-dependent birefringence of optical components between ODT coupler and the position of the atom, which influences the ODT polarization

- mechanical instability of the polarizer of ODT before the microscope objective, causing a change of polarization of the ODT

- drifts of the magnetic field compensation (see sec. 4.3).

Especially for the ODT polarization, a slightly elliptical polarization of $P = 0.01$ (from(3.8)), will result in a effective magnetic field of $257\,\mathrm{mG}$ at the trap center (from (3.13)) influencing the coherence of atomic states, which makes frequent calibration by experimentally measuring the evolution of atomic states indispensable. To analyze such measurements and draw the correct conclusions, in-depth knowledge of the experiment is crucial and the calibration process

is time consuming for the people working at the experiment. For those reasons a faster, yet precise method to calibrate the magnetic field compensation, that in future might even operate autonomously, is desirable.

The idea is to use a simulation of atomic state evolution for a given set of parameters, which yields a possible result of real measurement with these parameter, including the effective magnetic field. A dataset of such simulations for different effective magnetic fields can then be used to fit a actual measurement, in order to find out the $\vec{B}_{eff}(\vec{x}_{at})$ at the instance a measurement was taken. In the following, I will outline the way the simulation of atomic state evolutions works and list the important parameters going into this simulation. After that, I will explain what kind of measurement needs to be taken and how a $\vec{B}_{eff}(\vec{x}_{at})$ can be extracted.

5.1. Simulation of the evolution of atomic states

For a Monte-Carlo-type simulation of the evolution of atomic states, we need to recreate the experimental situation with all known parameters and effects. The parameters that have to be taken into account are:

- the initially prepared atomic state, which will be $|\Psi_V\rangle$ and $|\Psi_H\rangle$ as defined in section 3.1.1

- the trap geometry (Gaussian beam) that determines the range motion of the atom. The characteristic parameter is the waist of the dipole trap beam in the focal plane. The Rayleigh-length can be calculated from the waist with (2.4). Both could be obtained experimentally by knife-edge measurements [24]. An asymmetry of the trapping potential mentioned in [7] could not be observed whilst this work was performed, therefore it will be neglected.

- the trap depth U_0 that is proportional to the intensity of the dipole trap laser beam and determines the trapping frequencies Ω_r and Ω_z. Thereby it also determines the frequency of dephasing and rephasing of the atomic state due to the effects described in sec. 3.3

- the (local) ellipticity of polarization of the ODT beam leading to state evolutions caused by the AC Stark effect as described in Chap. 3. It can be characterized by the maximal effective magnetic field $B_{circ,max}$, which is at the focal spot, coming from this effect (see (3.12))

- the temperature T of the atoms, which determines the thermal distribution used to determine initial positions and velocities in the trap as mentioned above

- the static magnetic field $\vec{B}$ applied during the whole measurement, which is equal for all simulated trajectories

- fluctuations $\Delta\vec{B}$ of the magnetic field, that are individual to every single state evolution (see sec. 4.2, 4.3 and 4.4)

- the dark state $|\Psi_D\rangle$ of the atomic state readout after state evolution, which will be either $|\Psi_D\rangle = |\Psi_V\rangle$ or $|\Psi_D\rangle = |\Psi_H\rangle$

- the fidelity of the atomic state readout as described in 2.6 for measurements without a time delay/atomic state evolution.

The values of those parameters used for the simulation are listed in table 5.1 for the experimental setups in both labs.

The simulation than follows the steps that are performed in the experiment and simulates single atomic state evolutions. As there are position-dependent effects affecting the atomic state, we have to take into account the mechanical motion of the atom in the trap. Therefore the simulation starts with the initial conditions of the experiment, meaning the initially prepared atomic states, the starting position and starting velocity according to the thermal distribution and the magnetic field fluctuations. Finally an average over the single evolutions is performed. How to determine the starting conditions will be discussed in the following.

5.1.1. Mechanical motion of atoms in the trap

Here I follow a description given in [7]. The mechanical trajectory of the atom is treated in classical fashion, as a massive particle a Gaussian potential created by the ODT. In order to simulate a measurement, the trajectories of many atoms (typically 10000) have to be simulated with differing initial conditions. The initial conditions are both the position and velocity of the atom when it emits the single photon, the atom is entangled with. These initial conditions are calculated by assuming a three-dimensional harmonic oscillator as trapping potential, which creates negligible inaccuracies. Additionally the ambient magnetic field is a initial condition, as it differs slightly for every single atomic state evolution. The initial position of the atom in a harmonic oscillator are independent for each spatial direction and can be written as

$$x_0 = A_x \sin\left(\varphi_x\right)$$
$$y_0 = A_y \sin\left(\varphi_y\right)$$
$$z_0 = A_z \sin\left(\varphi_z\right)$$

where φ_i ($i \in \{x, y, z\}$) is a uniformly distributed random phase and A_i is a random amplitude of the harmonic oscillator, depending on the energy E as

$$E = \frac{1}{2} m_{Rb} \omega_i^2 A^2 \tag{5.1}$$

with m_{Rb} the atomic mass of ^{87}Rb and ω_i the the trap frequency along a given axis. The energy E is distributed according to a one dimensional Boltzmann distribution

$$\varrho\left(E\right) = \frac{1}{k_B T} \exp\left(-\frac{E}{k_B T}\right) \tag{5.2}$$

with k_B the Boltzmann constant and T the atomic temperature. Note that it is not a temperature in a macroscopic sense, as it is a single particle in the trap, but the ensemble of subsequent atoms will behave according to the thermal Boltzmann distribution. In order efficiently sample large number of A_i, we express them depending on a uniformly distributed random number `rand` $\in [0, 1]$. With the cumulative distribution of (5.2) being

$$
\begin{aligned}
F(E) &= \frac{1}{k_B T} \int_0^E dE' \exp\left(-\frac{E'}{k_B T}\right) \\
&= 1 - \exp\left(-\frac{E}{k_B T}\right)
\end{aligned}
\tag{5.3}
$$

and $F(E) \in [0, 1]$, we can invert (5.3) to $E = F^{-1}(\texttt{rand})$ and insert (5.1) leading to

$$
A_i = \sqrt{-\frac{2 k_B T}{m_{Rb} \omega_i^2} \ln(1 - \texttt{rand})}.
$$

With the radial symmetry of the trapping potential from sec. 2.3.1 (2.6), the trapping frequencies are

$$
\begin{aligned}
\omega_x &= \omega_y = \Omega_r \\
\omega_z &= \Omega_z.
\end{aligned}
$$

Accordingly, the initial velocities expressed by

$$
\begin{aligned}
v_{x,0} &= A_x \Omega_r \cos(\varphi_x) \\
v_{y,0} &= A_y \Omega_r \cos(\varphi_y) \\
v_{z,0} &= A_z \Omega_z \cos(\varphi_z).
\end{aligned}
$$

5.1.2. Magnetic field fluctuations

Additionally to the mechanical starting conditions, the magnetic field also has fluctuations specific for each state evolution. The ambient magnetic field $\vec{B}$, that the atom is exposed to during state evolution, is assumed to be constant during the time of a single state evolution. Instead we treat the fluctuations ΔB_i described in sec. 4.2 to 4.4 as 'shot-to-shot' fluctuations, giving a slightly different magnetic field for every single state evolution. All external fluctuations are assumed to normally distributed and independent from one another. For that reason we can combine them to one Gaussian distribution for each spatial direction given by

$$
\varrho_i(\Delta B_i) = \frac{1}{\sqrt{2\pi\sigma_{B,i}^2}} \exp\left(-\frac{(\Delta B_i)^2}{2\sigma_{B,i}^2}\right)
$$

with a standard deviation

$$\sigma_{B,i} = \sqrt{\left(\sigma_{HF}^{(i)}\right)^2 + \left(\sigma_{SR}^{(i)}\right)^2 + \left(\sigma_{IH}^{(i)}\right)^2}$$

as given in (4.2), (4.3) and (4.4) with experimental values noted in table 4.1. To numerically sample a Gaussian distribution efficiently, we can use the Box-Muller method [5]. It uses two uniformly distributed random numbers $\{u_1, u_2\} \in [-1, 1]$, that can be generated by $u_j = 2 \cdot \texttt{rand} - 1$ ($j \in \{1, 2\}$). They have to be inside of a unit circle with radius

$$r = \sqrt{u_1^2 + u_2^2} \leq 1.$$

Then the shot-to-shot magnetic field fluctuations

$$\Delta B_i = \sigma_{B,i} \cdot u_j \sqrt{-\frac{2\ln(r)}{r}}$$

are Gaussian distributed.

5.1.3. State simulation after initialization

The mechanical trajectory of a single atom is calculated as a classical massive particle in a Gaussian potential up to a final evolution time t_{fin} (typically up to $t_{fin} = 100\,\mu\text{s}$) with discrete timesteps Δt (typically $\Delta t = 100\,\text{ns}$). For each time step, the change of the atomic states is calculated. At a certain position $\vec{x}$, the atom is affected by a effective magnetic $\vec{B}_{eff}(\vec{x})$, that contains contributions of the ambient magnetic field $\vec{B}$, of the initial elliptical polarization of the ODT and effects of elliptical polarization due to focusing of the ODT as

$$\vec{B}_{eff}(\vec{x}) = \vec{B} + \frac{1}{\mu_B} P R_{circ} U_m(\vec{x})\,\vec{e}_z + B_{long}(\vec{x})\,\vec{e}_y$$

summarizes all effects on the atom as explained in Chapter 3. The program evaluates projections of the atomic state onto the dark state of the atomic state readout (typically $|\Psi_D\rangle = |\Psi_V\rangle$ or $|\Psi_D\rangle = |\Psi_H\rangle$) and averages over all trajectories giving a state population of the chosen dark state at any delay time t up to t_{fin}. This gives a result that can be compared directly to experimental measurements of the atomic state with a variable time delay. An example of such simulations for the parameters of lab 1 and lab 2 for a vanishing static magnetic field $\vec{B} = 0$ is presented in fig 5.1. A single run of such a simulation with 10000 simulated atomic state evolutions and a timestep $\Delta t = 100\,\text{ns}$ up to the maximal delay time $t_{fin} = 100\,\mu\text{s}$ takes 2-3 minutes on a mid-range office PC.

(a) Lab 1. For readout: $|\Psi_D\rangle = |\Psi_V\rangle$

(b) Lab 1. For readout: $|\Psi_D\rangle = |\Psi_H\rangle$

(c) Lab 2. For readout: $|\Psi_D\rangle = |\Psi_V\rangle$

(d) Lab 2. For readout: $|\Psi_D\rangle = |\Psi_H\rangle$
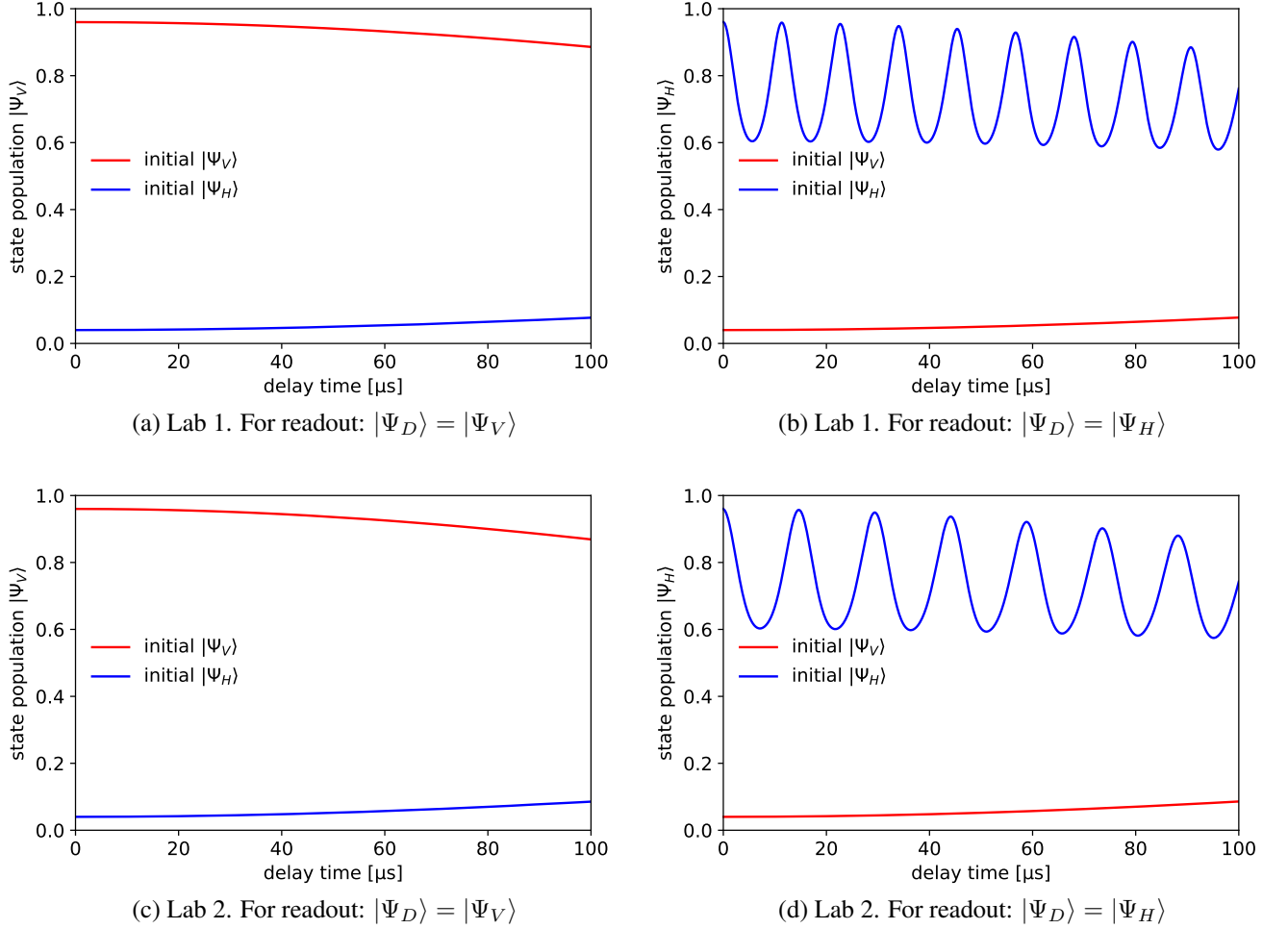
Figure 5.1.: Simulated atomic state evolutions for both labs with parameters as given in table 5.1 and a static magnetic field $\vec{B} = 0$. Only when projecting onto $|\Psi_D\rangle = |\Psi_H\rangle$ after a certain time delay, the effective magnetic field in y-direction caused by the oscillation of the atom in the tightly-focused ODT is recognizable. Note that the lower trap depth of lab 2 compared to lab 1 leads to slower dephasing and rephasing in lab 2. The difference was chosen a way, that for atom-atom entanglement experiments, we could measure in both traps with maximal possible contrast (i.e. at a rephasing point), when we take into account the time delays due to signal propagation from lab 1 to lab 2.

parameter	lab 1	lab 2
trap depth U_0	$k_B \cdot 2.98\,\text{mK}$	$k_B \cdot 1.80\,\text{mK}$
waist w_0	$1.9\,\mu\text{m}$	$1.9\,\mu\text{m}$
atomic temperature T	$30\,\mu\text{K}$	$30\,\mu\text{K}$
elliptical polarization $B_{circ,max}^{(*)}$	$0.035\,\text{mG}$	$0.035\,\text{mG}$
magnetic field fluctuations $\sigma_{B,x}$	$0.86\,\text{mG}$	$0.65\,\text{mG}$
magnetic field fluctuations $\sigma_{B,y}$	$0.41\,\text{mG}$	$0.35\,\text{mG}$
magnetic field fluctuations $\sigma_{B,z}$	$0.51\,\text{mG}$	$0.57\,\text{mG}$

Table 5.1.: Parameters of the setups in lab 1 and lab 2 used for simulation of atomic state evolutions as described in sec. 5.1. $^{(*)}$The elliptical polarization is set to (nearly) 0 by assumption. This not the case in the experimental setup, for fits this effect will contribute to the magnetic field $\vec{B}$.

5.1.4. Determining atomic temperature

The atomic temperature (or thermal energy of the atoms) is an important parameter in the context of the dynamics in the trap. It determines the width of the initial position distribution and the initial velocity distribution of subsequently trapped atoms as given in (5.3). Thereby the temperature determines how far the atoms will enter into regions of high effective magnetic field in y-direction arising from focusing the ODT while oscillating in the trap and thereby the dephasing and rephasing effects described in sec. 3.3. For hotter atoms, this means that they will reach higher field areas (compare fig. 3.2), meaning that they Larmor precession is faster, which would lead to steeper incline to the peaks in fig 5.2. Additionally, hotter atoms will statistically move more far along the z-axis, which leads to a degradation of the rephasing, as acquired phases on the left-hand side of the y-z-plane, do cancel each other out less perfectly.

With the means of the simulation of atomic states' evolution, we can simulate measurements for different atomic temperatures and compare those to actual measurements of atomic state populations at time delays around a rephasing point, which lets us determine the actual atomic temperature. Such measurements and simulations for lab 1 and lab 2 are shown in fig. 5.2. For the experimental measurement the static magnetic field was optimized to be as close to $\vec{B} = 0$ as possible, in order to reduce the influence of state evolution due to Larmor precession to a minimum. From comparing measurements and simulation, we can determine the atomic temperature in both labs to be $T = 30 \pm 3\,\mu\text{K}$. For the simulation we used the parameters listed in table 5.1. The effect of initial elliptical polarization of the ODT (see sec. 3.2) influences the atomic state evolution temperature-dependently due to the temperature-dependent motion of the atom in the effective magnetic field created by this effect. For the analysis performed here it was neglected by asumption, as its parameter entering the simulation $B_{circ,max}$ was set to $B_{circ,max} = 35\,\mu\text{G}$.

(a) Lab 1. (b) Lab 2
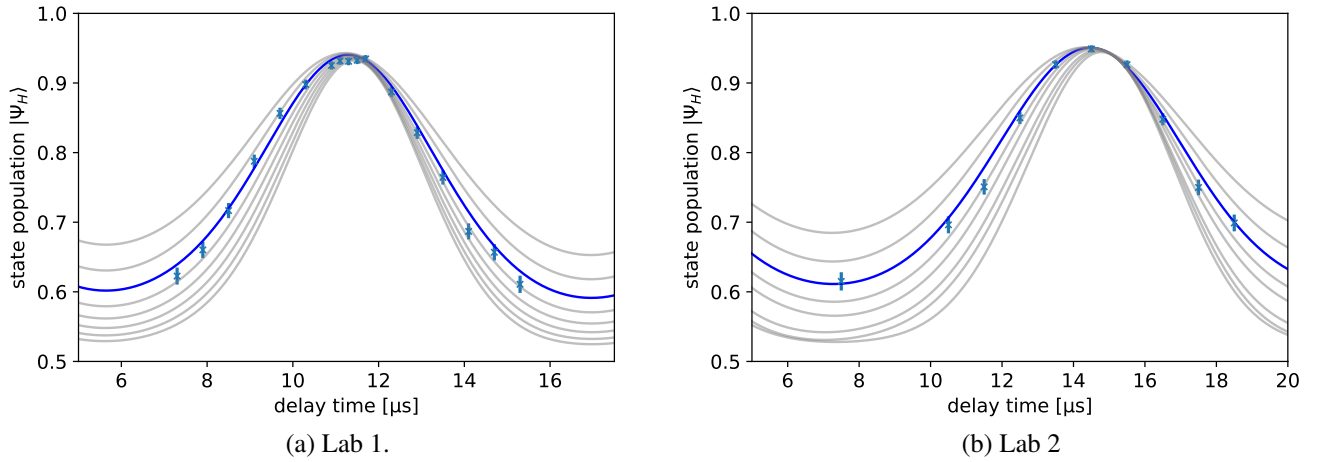
Figure 5.2.: Measurement of atomic temperatures in lab 1 (a) and lab 2 (b). In grey are simulations of temperatures from $20\,\mu$K (top) to $55\,\mu$K (bottom) in steps of $5\,\mu$K. The blue line corresponds to simulation for a temperature of $30\,\mu$K, which fits best to the measurements in both labs.

5.2. Analysis of atomic state measurements

With the simulation at hand that can predict the atomic state evolution for a certain set of parameters to a good degree, even for delay times up to $100\,\mu$s, one can now fit actual measurement data to the simulation in order the extract fitted parameters from the experiment. These extracted parameters can then be used to further adjust the parameters in the experiment. Here I will explain, how such an optimization for the magnetic field $\vec{B}$ can be realized.

As explained above, a reasonable simulation of atomic state evolution takes several minutes. This is too slow for a 'real-time' fitting procedure. Nevertheless, we can use a set of precalculated state evolutions as a database for fitting. This implies several requirements and limitations for the fitting procedure:

- Every parameter used in the simulation for a precalculated database (such as trap depth, beam waist, fluctuations of magnetic fields, ...) has to be stable on timescales larger than the time it takes to calculate the database and perform one or multiple fits of actual measurements.

- Resulting from the first requirement, a new database has to be created, if a parameter entering the simulation has changed.

- The precalculated database gives limits to ranges in which we can fit parameters, as these ranges have to be known before database creation, to avoid to large databases.

For fitting magnetic fields $\vec{B}$, these requirements can be met, especially as the magnetic field drifts by several mG on a timescale of hours and days, whereas the other parameters entering the

simulation listed in table 5.1 are longterm stable, or they are intentionally kept constant (e.g. for the trap depth U_0: the power of the optical dipole trap beam is stabilized to a constant value).

For an interval of magnetic fields that should be fitted, we limit ourselves to the most common use case, which is optimization of the magnetic field in intervals from 12 hours to three days. The expected magnetic field for this timescale is within

$$B_x, B_y, B_z \in [-10, 10] \text{ mG} \tag{5.4}$$

Cases how such state evolutions can look like are given in fig. 5.1 for both labs and $\vec{B} = 0$. An example for $\vec{B} = 5\,\text{mG} \cdot \vec{e}_z$ and $\vec{B} = 5\,\text{mG} \cdot \vec{e}_y$ is presented in fig. 5.3.

5.2.1. Experimental measurement scheme and evaluation procedure

To determine the complete magnetic field vector $\vec{B} = B_x\vec{e}_x + B_y\vec{e}_y + B_z\vec{e}_z$, we have to perform experimental measurements in two orthogonal directions of the atomic state readout (e.g. $|\Psi_D\rangle = |\Psi_V\rangle$ and $|\Psi_D\rangle = |\Psi_H\rangle$), as atomic state evolutions for some fields will not be detectable if using only one detection setting (compare to fig 5.3 and sec. 3.1.1).

Additionally the experimental measurement of atomic state evolutions is time consuming. The event rate for atom-photon entanglement events mainly depends on the loading rate of the ODT. The whole experimental procedure of pumping and exciting the atom and measuring the atomic state is performed in a few ten ms, but as the atomic state measurement is performed by state-selectively ionizing the atom, in 50% of the cases the atom is lost from the trap and a new atom has to be loaded, which takes 1 to 2 seconds. Therefore the event rate for typical experimental conditions is between 50 to 100 events per minute. This strongly limits the number of points and the statistics for each point we can measure in a given experimental time. In the following, we choose the atomic readout basis to be $|\Psi_D\rangle = |\Psi_V\rangle$ and $|\Psi_D\rangle = |\Psi_H\rangle$ and measure in both basis at delay times of

$$t_d \in [40, 50, 60, 70, 80, 90] \text{ μs.} \tag{5.5}$$

As we want to automate the task of evaluating an experimental measurement and finding $\vec{B}$, I here want to list the work flow and program logic briefly:

- After measuring experimental data according to the scheme mentioned above, the program needs to read in the data and sort and convert it accordingly, in order to get state populations for delay times t_d as displayed in fig. 5.3, which allow a comparison to simulated state populations. An important step is to determine the atom-in/atom-out threshold for fluorescence detection within the atomic state readout (sec. 2.5) in an automated fashion, which will be explained in sec.5.2.2.

- Then an initial guess for the fit parameters B_x, B_y, B_z has to be developed for the fitting procedure to be able to start fitting (see sec. 5.2.3)

(a) $\vec{B} = 5\,\text{mG} \cdot \vec{e}_z$, readout: $|\Psi_D\rangle = |\Psi_V\rangle$

(b) $\vec{B} = 5\,\text{mG} \cdot \vec{e}_z$, readout: $|\Psi_D\rangle = |\Psi_H\rangle$

(c) $\vec{B} = 5\,\text{mG} \cdot \vec{e}_y$, readout: $|\Psi_D\rangle = |\Psi_V\rangle$

(d) $\vec{B} = 5\,\text{mG} \cdot \vec{e}_y$, readout: $|\Psi_D\rangle = |\Psi_H\rangle$
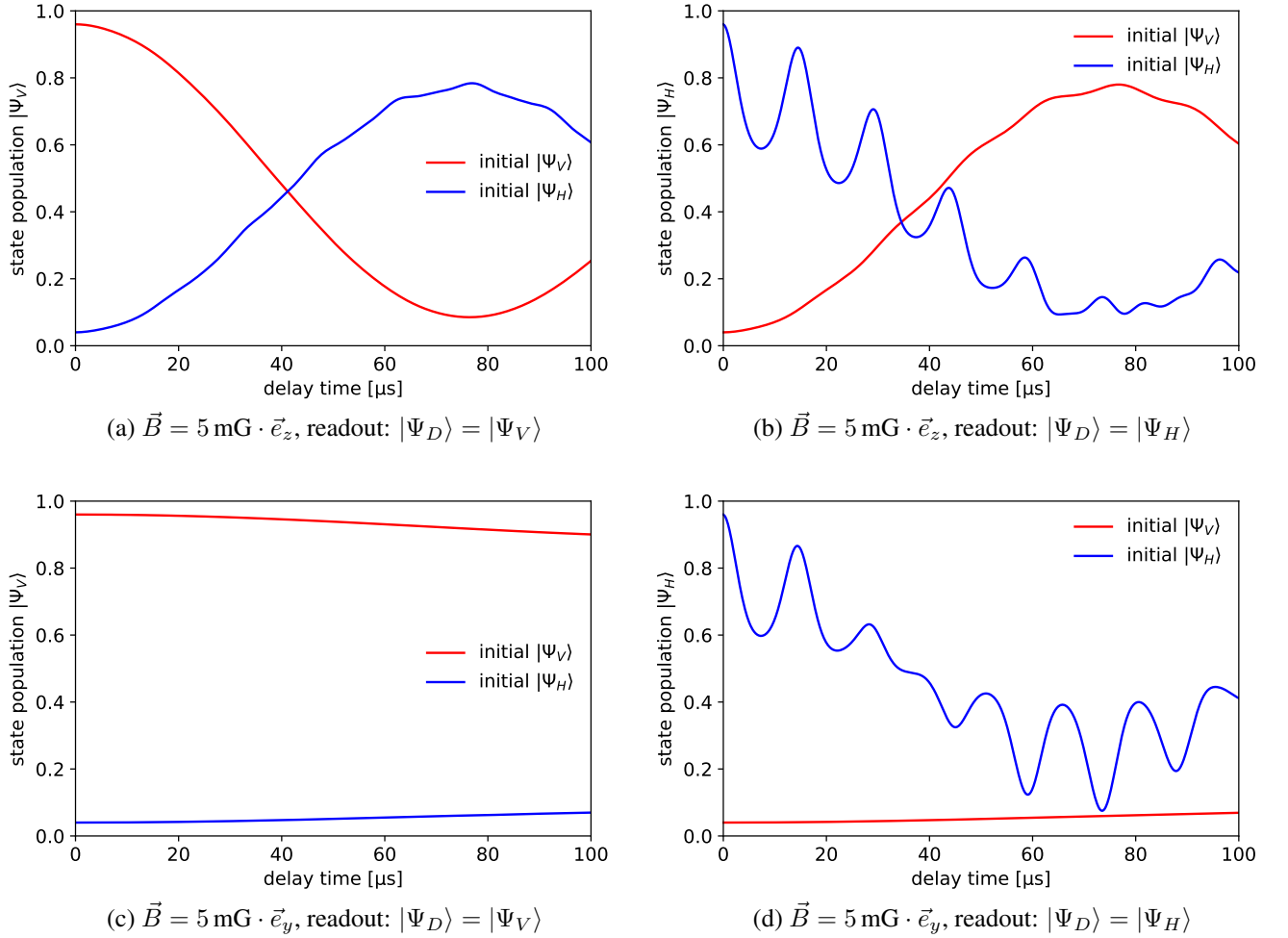
Figure 5.3.: Simulated atomic state evolutions for magnetic fields (a)+(b): $\vec{B} = 5\,\text{mG} \cdot \vec{e}_z$ and (c)+(d): $\vec{B} = 5\,\text{mG} \cdot \vec{e}_y$. All state evolutions were calculated for parameters of lab 2 according to table 5.1. When comparing this to fig. 5.1, note that a magnetic field in z-direction can be recognized in both analyzed states $|\Psi_D\rangle = |\Psi_V\rangle$ and $|\Psi_D\rangle = |\Psi_H\rangle$, while a magnetic field in y-direction can only be recognized in one analyzed state $|\Psi_D\rangle = |\Psi_H\rangle$ (and vice versa a field in x-direction only in analyzed state $|\Psi_D\rangle = |\Psi_V\rangle$).

- Following that, the fit has to be performed by an algorithm. One very important part there is the way the error function of the fit is defined and calculated (see 5.2.4)

- In the end the signs have to be determined by additional experimental measurements, as it is not possible to uniquely determine the orientation of B_x, B_y, B_z in one measurement (see sec. 5.2.5)

In the following, I will describe the methods used to fit the parameter $\vec{B}$ with the help of pre-calculated state evolutions to an experimental measurement in greater detail, the performance of this scheme is evaluated in sec. 5.3.

5.2.2. Atom-in/atom-out threshold

Since the atomic state readout scheme (sec. 2.5) is a Zeeman state-selective removal of the atom from the trap, it is necessary to determine whether the atom is lost or still trapped after the readout process. To do this, cooling and repump lasers are turned on for $65.5\,\mathrm{ms}$[24]. The detected photon counts during that time will indicate, whether the atom is lost (low background counts) or if it is still trapped (high fluorescence counts). Thereby we can determine whether an atom was ionized or not by setting a threshold for the number of photons counts c recorded during the defined time window. An example how such a histogram looks like is given in fig. 5.4. As we can see there the photon counts for 'atom in trap' and 'no atom in trap' are well described by a Gaussian distribution. Therefore we can fit

$$f(c) = C_{out} \cdot \exp\left(-\frac{(c - \mu_{out})^2}{2\sigma_{out}^2}\right) + C_{in} \cdot \exp\left(-\frac{(c - \mu_{in})^2}{2\sigma_{in}^2}\right) \tag{5.6}$$

to the experimental data, where C_{out} and C_{in} are scaling factors, σ_{out} and σ_{in} are the standard deviations and μ_{out} and μ_{in} are the offsets of the photon count distributions for 'no atom in trap' and 'atom in trap' respectively. In order to find the threshold of counts c_{thres} between 'no atom in trap' and 'atom in trap', we can calculate the minimum of (5.6) between its two maxima

$$c_{thres} = \min\left(f(c)\right)|\mu_{out} < c < \mu_{in}.$$

Therefore we can determine the threshold number of counts c_{thres} in a automated way.
With the help of the fit we can also estimate the error that we introduce by setting a threshold. Errors here would be events, where the atom is still in the trap, but the registered fluorescence count for this event is below c_{thres}, or vice versa a atom is expelled from the trap, but the event's fluorescence count is above c_{thres}. This typically only happens, if there is additional stray light collected by the collection optics (e.g. when reflexes of the cooling and repump light are collected) and thereby additional photon counts are created. When assuming Gaussian distributions with for both cases, a fit according to (5.6) gives the parameters to both distributions individually.

(a) Histogram and fit.

(b) Individual distributions and error estimation.
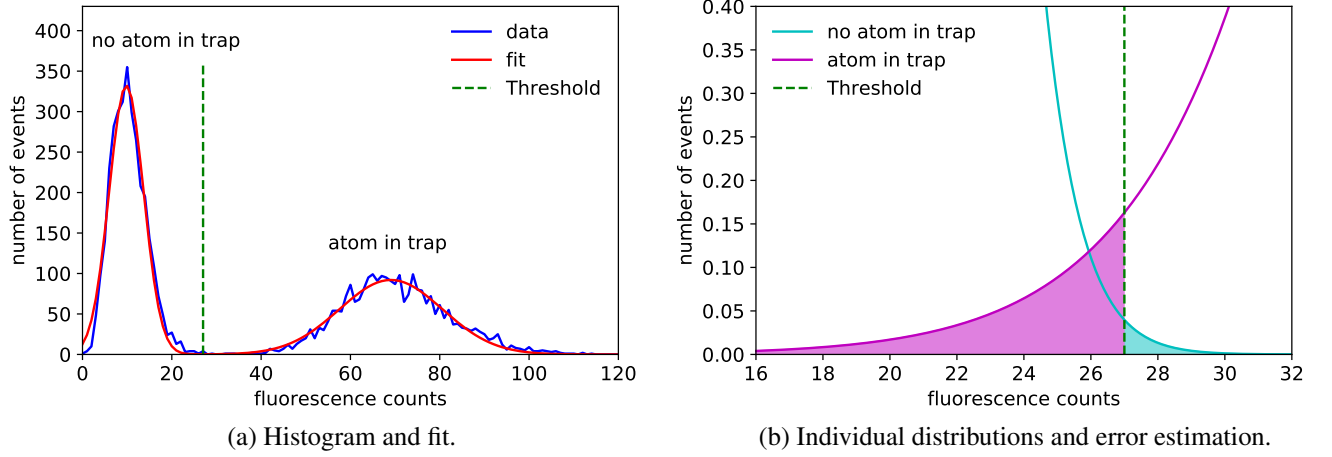
Figure 5.4.: (a): Histogram of photon counts during fluorescence detection, as part of the atomic state readout and the fit according to (5.6) for a measurement in lab 1. The photon count threshold, to distinguish between 'no atom in trap' and 'atom in trap' is $c_{thres} = 27$. (b): zoom into the region around c_{thres} of (a). The curves are expected distributions of photon counts of 'no atom in trap' and 'atom in trap' with fitted parameters from (5.6). The shaded areas are the expected errors due to the setting of the threshold.

We can therefore also estimate the errors e_{in} and e_{out} by integrating the tails of the individual distributions crossing c_{thres} as

$$e_{in} = \int_0^{c_{thres}} dc' \, C_{in} \cdot \exp\left(-\frac{(c' - \mu_{in})^2}{2\sigma_{in}^2}\right)$$

$$e_{out} = \int_{c_{thres}}^{\infty} dc' \, C_{out} \cdot \exp\left(-\frac{(c' - \mu_{out})^2}{2\sigma_{out}^2}\right)$$

and thus being recognized as the wrong event. A figure illustrating this can be found in fig. 5.4(b). The relative error then is

$$e_{rel} = \frac{e_{in} + e_{out}}{N_{tot}}$$

where N_{tot} is the total number of recorded events during one measurement. If the relative error $e_{rel} > 1\%$, the program will raise an error and stop further calculations.

5.2.3. Start parameters for fitting

The next step before fitting is to take an initial guess of the fit parameters B_x, B_y, B_z for the fitting algorithm to start with a set of parameters, that is as close as possible to the actual ones in order

to increase the probability of a successful fit. With the experimental measurement procedure described in sec. 5.2.1 and conversion of the measurement results into values commensurate with simulated evolution of states, we have 24 measured values in total, that can be grouped in four groups

$$
\begin{aligned}
d_{VV} &= \left\{ \| \langle \Psi_V | \, \Psi_V \, (t_d) \rangle \|^2 \right\} \\
d_{VH} &= \left\{ \| \langle \Psi_V | \, \Psi_H \, (t_d) \rangle \|^2 \right\} \\
d_{HV} &= \left\{ \| \langle \Psi_H | \, \Psi_V \, (t_d) \rangle \|^2 \right\} \\
d_{HH} &= \left\{ \| \langle \Psi_H | \, \Psi_H \, (t_d) \rangle \|^2 \right\}
\end{aligned}
\tag{5.7}
$$

where each $d_{ij} \in [0,1]$ correspond to populations of the dark state of atomic state readout i and initially prepared atomic state j, each measured at the 6 delays t_d as defined in (5.5). According to (3.2), we can write a magnetic field as a magnitude B and normalized field components b_x, b_y and b_z. We use this decomposition to estimate the magnitude and the orientation separately.

For the orientation of the magnetic field, we look at the state evolutions for different magnetic fields as described in sec. 3.1.1 and shown in fig. 3.1 and 5.3. These show the Larmor precession of initially prepared atomic states $|\Psi_V\rangle$ and $|\Psi_H\rangle$ in respective magnetic fields, also depending on the choice of the atomic state readout ($|\Psi_D\rangle = |\Psi_V\rangle$ or $|\Psi_D\rangle = |\Psi_H\rangle$). By taking average values of the d_{ij} we determine whether one magnetic field component is dominant compared to the others. The decision table is noted in table 5.2.

The magnitude B can be estimated by determining the period of the Larmor precession. As the Larmor frequency depends on the magnitude of the magnetic field as given in 3.3, the time it takes for state inversion e.g. from $|\Psi_V\rangle$ to $|\Psi_H\rangle$ with pure B_z-field (see (3.4)) is

$$
T = \frac{\pi \hbar}{2 \mu_B g_F B}.
$$

For that reason we search for the minimal delay time t_{min}, where either d_{VV} or d_{HH} have their global minimum. We then set the initial magnitude of the magnetic field to

$$
B = \frac{\pi \hbar}{2 \mu_B g_F t_{min}}.
$$

With this procedure, we have found the start parameters B_x, B_y, B_z for fitting.

5.2.4. Fitting and error function

In order to fit the parameters B_x, B_y, B_z to an experimental measurement, we need three main components. These components are

- a database of simulated evolutions of atomic states. The database incorporates the connection between atomic state populations and the fit parameters B_x, B_y, B_z.

field scenario	$\overline{d_{VV}}$	$\overline{d_{VH}}$	$\overline{d_{HV}}$	$\overline{d_{HH}}$	b_x	b_y	b_z
dominating b_x	< 0.75	< 0.25	< 0.25	> 0.75	$\frac{2}{\sqrt{5}}$	$\frac{1}{\sqrt{10}}$	$\frac{1}{\sqrt{10}}$
dominating b_y	> 0.75	< 0.25	< 0.25	< 0.75	$\frac{1}{\sqrt{10}}$	$\frac{2}{\sqrt{5}}$	$\frac{1}{\sqrt{10}}$
dominating b_z	< 0.75	> 0.25	> 0.25	< 0.75	$\frac{1}{\sqrt{10}}$	$\frac{1}{\sqrt{10}}$	$\frac{2}{\sqrt{5}}$
equal fields	non of the above				$\frac{1}{\sqrt{3}}$	$\frac{1}{\sqrt{3}}$	$\frac{1}{\sqrt{3}}$

Table 5.2.: Decision table for orientation of $\vec{B}$ as the start parameters for fitting. $\overline{d_{ij}}$ are the averaged values of the experimentally measured d_{ij}. The threshold values of $\overline{d_{ij}}$ for each field scenario were determined by heuristic observation.

- an error function, that calculates the residual difference between experimentally measured state populations and simulated state populations for a certain magnetic field $\vec{B}$ and thereby defines a measure for the goodness of the fit.

- an algorithm, that performs the fit, i.e. minimizes the error function. If the minimization converges, the latest magnetic field $\vec{B}$ becomes the fitted magnetic field $\vec{B}_{fit}$.

Database

For the database we use the simulation described in sec. 5.1, where we simulate 10000 single evolutions of atomic states to the maximal delay time $t_{fin} = 100\,\mu s$ with a timestep $\Delta t = 100\,ns$ and average the simulated measurement results. These parameters of the simulation have shown an appropriate compromise between precision of the simulation and computation time. As the magnetic field components B_x, B_y, B_z are free parameters for the fit, we perform a simulation as mentioned above for every magnetic field configuration within $B_x, B_y, B_z \in [-10, 10]$ mG with a resolution of $\Delta B_i = 0.5$ mG. The database can then provide simulated atomic state populations

$$s_{VV}\left(\vec{B}, t\right) = \left\{ \left\| \langle \Psi_V | \Psi_V \left(\vec{B}, t\right) \rangle \right\|^2 \right\}$$

$$s_{VH}\left(\vec{B}, t\right) = \left\{ \left\| \langle \Psi_V | \Psi_H \left(\vec{B}, t\right) \rangle \right\|^2 \right\}$$

$$s_{HV}\left(\vec{B}, t\right) = \left\{ \left\| \langle \Psi_H | \Psi_V \left(\vec{B}, t\right) \rangle \right\|^2 \right\}$$

$$s_{HH}\left(\vec{B}, t\right) = \left\{ \left\| \langle \Psi_H | \Psi_H \left(\vec{B}, t\right) \rangle \right\|^2 \right\} \tag{5.8}$$

where each $s_{ij} \in [0, 1]$ corresponds to simulated populations of the dark state of atomic state readout i and initially prepared atomic state j after evolution for time $t \in [0, 100]$ μs in magnetic field $\vec{B}$, analogously to (5.7).

Error function

The error function has to give a measure to the residual difference between the experimental measurement and simulated evolution of atomic states for a certain magnetic field $\vec{B}$ that should be tested during the fit process. As the fit algorithm also works with gradients of the fit parameters, the error function has to be smooth, as for the test of $\vec{B}$ the error function will be evaluated four times, once directly at $\vec{B}$ and additionally at

$$\vec{B}_{gr,i} = \vec{B} + \delta B \cdot \vec{e}_i$$

where $i \in \{x, y, z\}$ and δB is a small change of the magnetic field on the order of 10^{-3} mG. Therefore the challenge now is to create a smooth error function, although the database is sampled in discrete steps $\Delta B_i = 0.5$ mG large compared to δB. We use means of linear interpolation to fill the gap between the simulations of evolution of atomic states in the database. For any simulated state population $s_{ij}(\vec{B}, t)$ (from (5.8)) required during the calculation of the error function, there are eight simulated state evolutions stored in the database, surrounding $s_{ij}(\vec{B}, t)$ in the $\vec{B}$ parameter space with a maximal deviation $\Delta B_i = 0.25$ mG. A three-dimensional linear interpolation function is used to deduce $s_{ij}(\vec{B}, t)$ from the nearest simulated state evolutions stored in the database.

The measure for the residual difference between measurement and simulation for a given $\vec{B}$ then is

$$err\left(\vec{B}\right) = \sum_t \sum_{i,j} \left| d_{ij}\left(t\right) - s_{ij}\left(\vec{B}, t\right) \right|^2 \tag{5.9}$$

where $t \in t_d$ are the time delays at which the experimental data was measured, $d_{ij}(t)$ is the measured state population (from (5.7)) and $s_{ij}(\vec{B}, t)$ is the simulated state population with $i, j \in \{H, V\}$.

Fitting algorithm

The fitting algorithm performs its task by starting with values for the magnetic field as determined in sec. 5.2.3 and then minimizing $err(\vec{B})$, yielding in the end the fitted magnetic field $\vec{B}_{fit}$. This algorithm also has to obey the boundary conditions set by the range of magnetic fields contained in the database given in (5.4). A suitable algorithm for this is the 'trust region reflective' (trf) algorithm [6]. It basically is like a Levenberg-Marquardt algorithm, where $err(\vec{B})$ is iteratively approximated by a quadratic hyperplane around the initial guess for $\vec{B}$, then a linear solver searches within this quadratic hyperplane for a minimum of $err(\vec{B})$, which is then used to update the estimate for $\vec{B}$ [21, 23]. The trf algorithm additionally implements boundaries and estimates, that would exceed the boundaries, are instead reflected at the boundaries . On top of that, the trf algorithm implements a trust region, in which it allows to estimate to change during

(a) Data and fit. Readout: $|\Psi_D\rangle = |\Psi_V\rangle$ (b) Data and fit. Readout: $|\Psi_D\rangle = |\Psi_H\rangle$
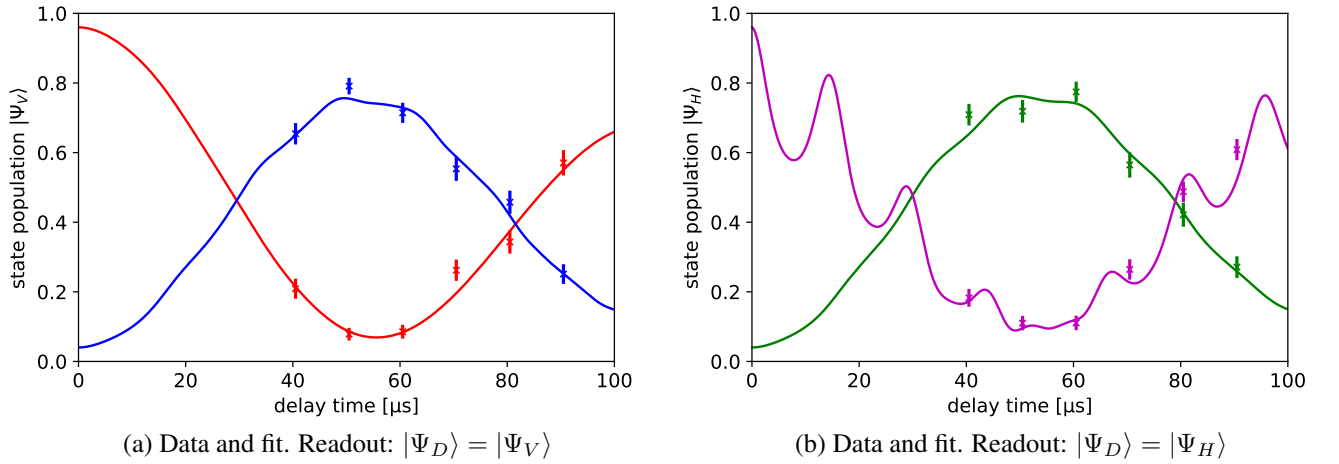
Figure 5.5.: Example of measurement data and fit of magnetic fields for lab 2 according to procedure described in sec. 5.2. The fitted magnetic field is $\vec{B}_{fit} = (0.12, 1.51, 6.99)$ mG. (a): Displayed is experimentally measured data d_{VV} (red crosses) and d_{VH} (blue crosses) and corresponding simulated state evolutions $s_{VV}(\vec{B}_{fit})$ (red solid line) and $s_{VV}(\vec{B}_{fit})$ (blue solid line). The readout direction is $|\Psi_D\rangle = |\Psi_V\rangle$. (b): Experimentally measured data d_{HH} (magenta crosses) and d_{HV} (green crosses) and corresponding simulated state evolutions $s_{HH}(\vec{B}_{fit})$ (magenta solid line) and $s_{HV}(\vec{B}_{fit})$ (green solid line). The readout direction is $|\Psi_D\rangle = |\Psi_H\rangle$. All d_{ij} as defined in (5.7) and all s_{ij} as defined in (5.8).

one iteration. This trust region is reduced continuously, if the estimate of $\vec{B}$ gets closer to the boundaries. This prevents the trf algorithm from getting stuck at the boundaries. In a nutshell the trf algorithm is a fast and robust algorithm for the minimization of $err(\vec{B})$ obeying the boundary conditions, resulting in a fitted magnetic field $\vec{B}_{fit}$.

A strong liability still are the starting parameters for the fit as estimated in sec. 5.2.3. If the residual relative error after optimization

$$err_{rel} = \frac{err\left(\vec{B}_{fit}\right)}{n_{t_d}}$$

where n_{t_d} is the number of time points, is larger than the a threshold of $err_{rel} > 5 \cdot 10^{-3}$, it has proven useful to start the optimization process all over again, with new starting parameters B_x, B_y, B_z, now randomly distributed within the boundaries. This step can be repeated multiple times, until $err_{rel} \leq 5 \cdot 10^{-3}$. An example of such a fit to experimentally measured data of lab 2 can be found in Fig. 5.5.

5.2.5. Determining the orientation of the magnetic field vector

To find the orientation of the fitted magnetic field vector $\vec{B}_{fit}$ is a challenging task on its own. We therefore have to determine the signs of the components B_x, B_y and B_z. If all components are contributing considerably to $\vec{B}_{fit}$, there are differences of atomic state populations for different parity of signs ('even (0 or 2) or uneven (1 or 3) number of minus signs within B_x, B_y, B_z'). Different parity of signs will change the orientation of the vector of Larmor precession in a way, that measurable state populations change, although the Larmor frequency ω_L (from (3.3)) stays the same. By performing a experimental measurement and evaluating the state populations as described in sec. 5.2.1 and sec. 5.2.4, we will not be able to determine the orientation of $\vec{B}_{fit}$ uniquely. Therefore, we take an iterative approach to finding out the orientation of $\vec{B}_{fit}$. With a $\vec{B}_{fit}$ from a fit as described above at hand, we start with the largest field contribution $B_{fit}^{(i)}$ ($i \in \{x, y, z\}$). If we now change $B^{(i)}$ at the experiment by a defined value in a certain direction

$$\Delta B^{(i)} = \frac{\Delta U_{ref}^{(i)}}{s^{(i)}}$$

with $U_{ref}^{(i)}$ the reference voltage of the magnetic feedback loop as described in sec. 4.1 and the sensitivity of the feedback loop sensor as given in (4.1), we can look at the expected state evolutions for both possible magnetic field configurations

$$\vec{B}_{new} = \vec{B}_{fit} \pm \Delta B^{(i)} \cdot \vec{e}_i.$$

From the database used for fitting we can extract, what state evolutions we expect for setting $\vec{B}_{new}$. With that, we can determine the delay time and the setting of the state readout we have to choose to be able to distinguish the best between both possibilities of $\vec{B}_{new}$. An image illustrating this process can be found in Fig. 5.6. We then have to experimentally measure at the proposed time delay whilst changing $\Delta U_{ref}^{(i)}$ by the defined amount in a certain direction. The measured state population then determines the sign of $B_{fit}^{(i)}$. This process then has to be repeated for the remaining components $B_{fit}^{(i)}$.

5.3. System performance

Sec. 5.2 described a way, how to measure and how to analyze a time-delayed atomic state population measurement for finding out the magnetic field configuration. An interesting question now is the performance of the analysis part, i.e. how precise is the analysis, meaning how accurate can $\vec{B}_{fit}$ be extracted. The simulation of evolution of atomic states explained in sec. 5.1, presents an optimal tool to test the analysis functionality with synthetic data. Synthetic data stands for data, that was not taken by experimental measurement, but by simulation with (low) statistics as

(a) Readout: $|\Psi_D\rangle = |\Psi_V\rangle$ (b) Readout: $|\Psi_D\rangle = |\Psi_H\rangle$
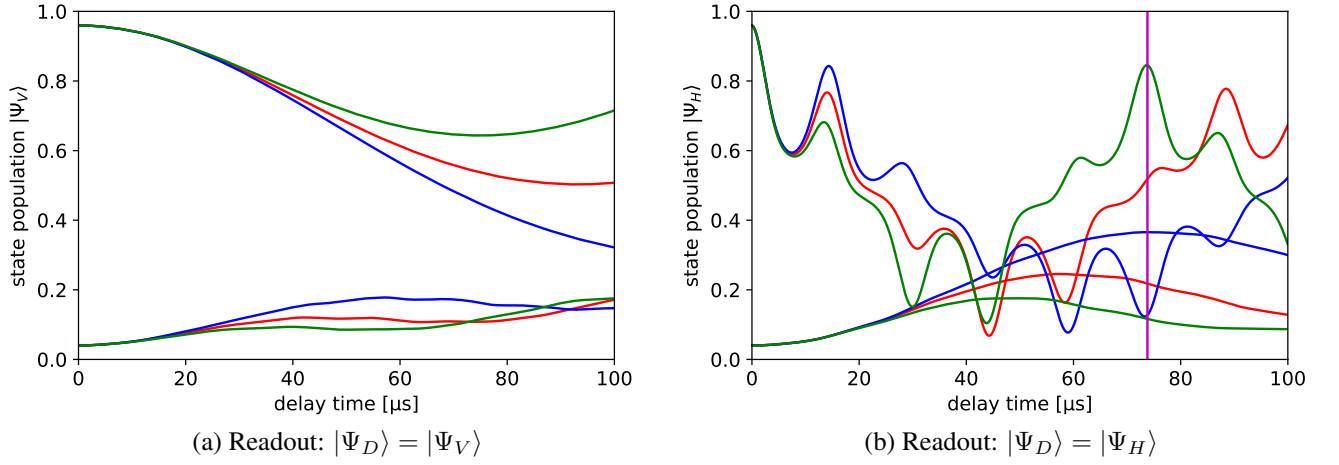
Figure 5.6.: State evolutions for $\vec{B}_{fit} = (1, 7, 3)$ mG (red), $\vec{B}_{new,+} = \vec{B}_{fit} + 2\,\text{mG}\cdot\vec{e}_y$ (green) and $\vec{B}_{new,-} = \vec{B}_{fit} - 2\,\text{mG}\cdot\vec{e}_y$. The delay time where to measure best for the direction of B_y is at $t_d = 73.8\,\mu$s with readout $|\Psi_D\rangle = |\Psi_H\rangle$ as indicated by the vertical magenta line. There the state population of initial state $|\Psi_H\rangle$ for $\vec{B}_{new,-}$ and $\vec{B}_{new,+}$ differ the most.

experimental measurement would yield. Another advantage of synthetic data, is the full knowledge and control about all parameters entering the simulation, whereas in a real experiment, the control over parameters is limited and some parameters are hard to determine. For the following performance test, we will limit ourselves to three typical magnetic field configurations, as the following analysis is heavy in computation. For magnetic field configurations we choose:

- equal fields in all spatial directions $\vec{B}_{input} = (5, 5, 5)$ mG

- a dominating field contribution in z-direction, with smaller contributions of other field components $\vec{B}_{input} = (0.5, 1, 7)$ mG

- small contributions from all components $\vec{B}_{input} = (1, 1, 1)$ mG

A second advantage of the simulation is, that it simulates a measurement in exactly the same steps, as the experimental setup would perform a measurement as well. The accuracy of a measurement at the experimental setup is largely limited by the statistics we can accumulate in a certain time. For atom-photon entanglement events, the current experimental rate is in the range of 50 to 100 events per minute. Hence, a measurement as described in sec. 5.2.1, would take take 1 to 2 hours to acquire on average 250 events per datapoint. This gives a guideline on how to to test the analysis functionality. We use the simulation of evolution of atomic states with event numbers per datapoint of

$$n_{ev} = \{100, 200, 400, 600, 800, 1000, 1200, 1400\} \tag{5.10}$$

(a) Histogram of $B_{fit}^{(y)}$ for $n_{ev} = 100$

(b) Fit accuracy for $\vec{B}_{input} = (5, 5, 5)$ mG

(c) Fit accuracy for $\vec{B}_{input} = (0.5, 1, 7)$ mG

(d) Fit accuracy for $\vec{B}_{input} = (1, 1, 1)$ mG
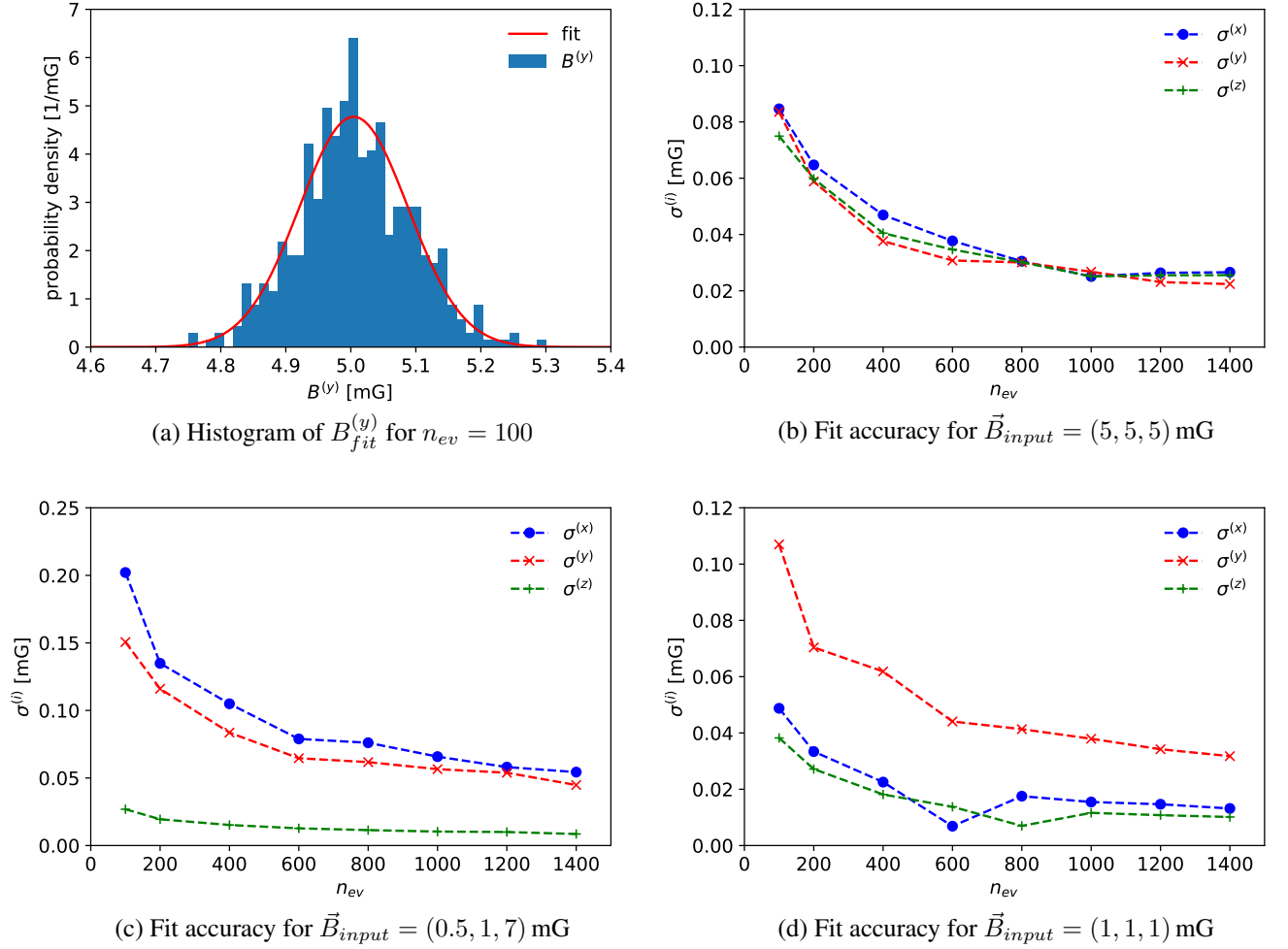
Figure 5.7.: (a): Histogram of fitted magnetic field values $B_{fit}^{(y)}$ in a field configuration of $\vec{B}_{input} = (5, 5, 5)$ mG, where the statistics of the synthetic input were limited to $n_{ev} = 100$. (b)+(c)+(d): Figure of merit $\sigma_{fit,n_{ev}}^{(i)}$ as defined in (5.7) for limited statistics n_{ev}. Note that in (c) the dominating field contribution in z-direction was detected very precisely, while the smaller contributions had a large scatter compared to the field configuration in (b) and (d).

which are rather small compared to 10000 simulated events used for the creation of the database. The simulation with those limited statistics is repeated multiple times, to simulate different experimental realizations of the same kind, as the statistical distributions sampled in every simulation run will sample different starting conditions, as if it were different experimental realizations. Drawing from those simulated experimental realizations, we can generate synthetic data as input of the analysis tool, that in principle should output the magnetic field, that was the input in the simulation ($\vec{B}_{fit} = \vec{B}_{input}$). This is in general not exactly the case, as the synthetic data is simulated with very limited statistics, leading to fluctuations of the synthetic datapoints d_{ij}. Therefore the fitted magnetic field $\vec{B}_{fit}$ will have a certain scatter. This scatter can be represented in a normalized histogram (see Fig.5.7(a)). Gaussian distributions defined as

$$\varrho_{n_{ev}}^{(i)}\left(\Delta B_{fit,n_{ev}}^{(i)}\right) = \frac{1}{\sqrt{2\pi\left(\sigma_{fit,n_{ev}}^{(i)}\right)^2}}\exp\left(-\frac{\left(\Delta B_{fit,n_{ev}}^{(i)} - \mu\right)^2}{2\left(\sigma_{fit,n_{ev}}^{(i)}\right)^2}\right) \tag{5.11}$$

where $i \in \{x, y, z\}$ and n_{ev} as defined in (5.10), are fitted to the histograms. The standard deviation $\sigma_{fit,n_{ev}}^{(i)}$ of those fits is a good figure of merit for the analysis functionality working under the constraint of data with very limited statistics. The dependence of $\sigma_{fit,n_{ev}}^{(i)}$ on n_{ev} for three different magnetic field configurations $\vec{B}_{input}$ as mentioned above is shown in Fig. 5.7.

This test yields a good estimation about the expected accuracy of the fitting procedure, when dealing with limited statistics of a measurement. Yet this test will overestimate the fit accuracy, as all parameters (list of parameters in sec. 5.1) chosen to simulate a synthetic measurement are exactly the same as they are for the simulation of the database that is used for fitting. Such accordance of all parameters will not be the case for a real experimental measurement.

Nonetheless are the results shown in Fig. 5.7 very promising. With the experimental event rate being at 50 to 100 events per minute, a measurement time of 2 hours gives statistics of $250 \leq n_{ev} \leq 500$, which should enable us to determine $\vec{B}$ up to deviations of $\Delta\vec{B} \leq \pm 0.5\,\text{mG}$. Tests with real experimental data need to be performed. One test is to gauge the magnetic fields manually with the old procedure, then a measurement and fit executed as described in this chapter should yield $\vec{B} = \vec{0}$ up to the expected accuracy of the procedure.

5.4. Summary

In conclusion this chapter shows a way how to efficiently optimize the magnetic fields in a single atom experiment. The main components needed for this procedure are a precise simulation of evolution of atomic states in an optical dipole trap including all relevant effects, an up-to-date knowledge of the slowly-changing parameters of the experiment listed in table 5.1 and a functionality analyzing the measurement as described above. Up-to-date knowledge of the experimental parameters has to be obtained in separate measurements. Additional computational power is needed to create the database for fitting. The analysis functionality is developed to a

point, where it shows great promise to perform optimizations of the magnetic field to $B \leq \pm 0.5\,\mathrm{mG}$ in less than 1.5 hours, although a final experimental proof is still pending.

6. Conclusion and Outlook

This work describes a scheme to efficiently control the magnetic fields in experiments with single trapped ^{87}Rb atoms. This control is essential to ensure long term stability of magnetic fields over days which is necessary to achieve a high coherence of atomic states in data sets collected in long experimental runs.

The first part of the thesis describes in detail the effects leading to a time evolution of the atomic quantum state. The atomic quantum state stored in Zeeman states of the atomic hyperfine ground level is particularly influenced by external magnetic fields and the state-dependent AC-Stark shift induced by the light of the optical dipole trap which both lead to a Larmor precession of the atomic state. These two effects can be compensated by applying an additional magnetic field that compensates them. As presented in this thesis, such compensation reduces the fluctuations of the magnetic field down to a level of $\sigma_{\vec{B}} \approx 1\,\text{mG}$ (standard deviation) on a 'shot-to-shot' timescale (i.e. between single experiments), if the magnetic compensation setup is properly calibrated. This is sufficient to perform atom-atom entanglement experiments over a distance of $400\,\text{m}$ like a test of Bell's inequality closing all essential loopholes [30].

The second part discusses the calibration process of the magnetic field compensation. As experimental parameters affecting state coherence (e.g. the polarization of the dipole trap beam) drift on a hourly timescale, a calibration of the magnetic field compensation by efficiently measuring atomic state evolutions and deducing all components of the magnetic field from the measurement is indispensable. Therefore, a scheme is developed that performs such measurement analysis in an automated way under the condition of limited experimental data available for an efficient experimental implementation. It uses simulated state evolutions to fit measured atomic state evolutions with the magnetic field as a fit parameter. This fit assisted scheme shows great promise to calibrate the compensation setup to less than $0.5\,\text{mG}$ of static magnetic field within 1.5 hours, which is at least as precise and faster than a calibration that otherwise needs to be performed manually by experienced experimentalists. Therefore it can be performed more frequently, leading to an overall improved state coherence for long term experimental runs of atom-atom entanglement experiments.

Outlook

The analysis functionality for measurements of atomic state evolution developed throughout this work has to be tested thoroughly under experimental conditions. Therefore, the quality of calibration of the compensation setup has to be validated by comparing it to results which can be

achieved manually. With proven correctness of the automated analysis functionality, the whole procedure of calibrating the compensation setup can be automated even to the point where this optimization is performed completely autonomously. Therefore, additional interfaces in the software running and evaluating the experiment are necessary that allow for autonomous execution and analysis of experiments. In that way, the calibration of magnetic fields can be performed more efficiently without the need of supervision.

In addition, further improvements to increase the atomic state coherence have to be implemented in order to be able to perform experiments over distances of up to $20\,\text{km}$ as planned for the future. Those can include further development of the feedback loop setup for the magnetic field compensation by using a different sensor and larger compensation coils as discussed in sec. 4.5. Furthermore, the magnetic field compensation setup could be upgraded by using a more sophisticated feed-forward system that incorporates a detailed model of magnetic fields around the atom trap and uses input from multiple sensors. Together with using other states of the ^{87}Rb atom to encode the qubit making the qubit less sensitive to magnetic fields, these improvements would allow to increase the effective coherence time of the internal atomic states by several orders of magnitude.

A. Definition of coordinate system, polarization and atomic states

This appendix will give a short overview about some definitions that are made to consistently describe the coordinate system and reference frames for photonic polarization states and atomic Zeeman states. These definitions apply for both traps in the same way. This is a shortened and adapted version of the definitions given in the appendix of [26].

In this experiment a right-handed coordinate system is used. The origin of the coordinate system is the focal spot of the optical dipole trap (ODT). The z-axis is defined by the optical axis of the microscope objective, that creates the focus for the ODT and points from the origin towards the microscope objective. The y-axis is pointing in vertical direction and the x-axis is parallel to the optical table (horizontal plane).

The polarization of a photon is always defined with respect to the propagation direction of the photon. As the z-axis is the quantization axis in this experiment due to the single photons emitted by the atom being collected by the microscope objective (along the z-axis) all polarizations states of light in the lab framework ($|H\rangle$, $|V\rangle$, $|+\rangle$, $|-\rangle$, $|R\rangle$, $|L\rangle$) are given with respect to this reference, e.g. horizontally polarized light $|H\rangle$ describes light polarized in the x-z-plane.

In the reference frame of the atom the polarization of a photon emitted by the atom with a quantization axis Γ is defined as $|\sigma^+\rangle$(right-hand rotating in direction of travel), if $\Delta m_{F,\Gamma} = -1$ or $|\sigma^-\rangle$ (left-hand rotating in direction of travel), if $\Delta m_{F,\Gamma} = +1$ or $|\pi\rangle$ (linear polarization parallel to Γ), if $\Delta m_{F,\Gamma} = 0$.

The atomic qubit states are $|F = 1, m_F = -1\rangle_z$ ($|\downarrow\rangle_z$) and $|F = 1, m_F = +1\rangle_z$ ($|\uparrow\rangle_z$) which leads to the following relations, if we consider the above-mentioned definitions:

$$
\begin{aligned}
|\uparrow\rangle_x &= \frac{1}{\sqrt{2}} \left(|\downarrow\rangle_z + |\uparrow\rangle_z \right) \\
|\downarrow\rangle_x &= \frac{i}{\sqrt{2}} \left(|\downarrow\rangle_z - |\uparrow\rangle_z \right) \\
|\uparrow\rangle_y &= \frac{1}{\sqrt{2}} e^{i\frac{\pi}{4}} \left(|\downarrow\rangle_z - i |\uparrow\rangle_z \right) \\
|\downarrow\rangle_y &= \frac{1}{\sqrt{2}} e^{-i\frac{\pi}{4}} \left(|\downarrow\rangle_z + i |\uparrow\rangle_z \right)
\end{aligned}
\tag{A.1}
$$

Bibliography

[1] A. Acín, N. Brunner, N. Gisin, S. Massar, S. Pironio, and V. Scarani. Device-independent security of quantum cryptography against collective attacks. *Physical Review Letters*, 98(23):230501, 2007.

[2] E. A. Aguilar, R. Ramanathan, J. Kofler, and M. Pawłowski. Completely device-independent quantum key distribution. *Physical Review A*, 94(2):022305, 2016.

[3] C. H. Bennett, G. Brassard, C. Crépeau, R. Jozsa, A. Peres, and W. K. Wootters. Teleporting an unknown quantum state via dual classical and einstein-podolsky-rosen channels. *Physical review letters*, 70(13):1895, 1993.

[4] B. B. Blinov, D. L. Moehring, L.-M. Duan, and C. Monroe. Observation of entanglement between a single trapped atom and a single photon. *Nature*, 428(6979):153, 2004.

[5] G. E. P. Box. A note on the generation of random normal deviates. *Ann. Math. Stat.*, 29:610–611, 1958.

[6] M. A. Branch, T. F. Coleman, and Y. Li. A subspace, interior, and conjugate gradient method for large-scale bound-constrained minimization problems. *SIAM Journal on Scientific Computing*, 21(1):1–23, 1999.

[7] D. Burchard. *A Rigorous Test of Bells Inequality and Quantum Teleportation Employing Single Atoms*. PhD thesis, 2018.

[8] S. Chu, J. E. Bjorkholm, A. Ashkin, and A. Cable. Experimental observation of optically trapped atoms. *Physical review letters*, 57(3):314, 1986.

[9] S. Chu, L. Hollberg, J. E. Bjorkholm, A. Cable, and A. Ashkin. Three-dimensional viscous confinement and cooling of atoms by resonance radiation pressure. *Phys. Rev. Lett*, 1985.

[10] K. L. Corwin, S. J. M. Kuppens, D. Cho, and C. E. Wieman. Spin-polarized atoms in a circularly polarized optical dipole trap. *Physical review letters*, 83(7):1311, 1999.

[11] J. Dalibard and C. Cohen-Tannoudji. Laser cooling below the doppler limit by polarization gradients: simple theoretical models. *JOSA B*, 6(11):2023–2045, 1989.

[12] A. K. Ekert. Quantum cryptography based on bell's theorem. *Physical review letters*, 67(6):661, 1991.

[13] R. Grimm, M. Weidemüller, and Y. B. Ovchinnikov. Optical dipole traps for neutral atoms. *Advances in Atomic Molecular and Optical Physics*, 2000.

[14] T. W. Hänsch and A. L. Schawlow. Cooling of gases by laser radiation. *Optics Communication*, 1975.

[15] F. Henkel. *Photoionisation detection of single 87 Rb-atoms using channel electron multipliers*. PhD thesis, 2011.

[16] J. Hofmann. *Heralded Atom-Atom Entanglement*. PhD thesis, 2014.

[17] J. Hofmann, M. Krug, N. Ortegel, L. Gérard, M. Weber, W. Rosenfeld, and H. Weinfurter. Heralded entanglement between widely separated atoms. *Science*, 337(6090):72–75, 2012.

[18] C.-K. Hong, Z.-Y. Ou, and L. Mandel. Measurement of subpicosecond time intervals between two photons by interference. *Physical review letters*, 59(18):2044, 1987.

[19] T. Hummel. Increasing photon collection efficiency for generating long-distance entanglement of atoms. Master's thesis, 2018.

[20] M. Krug. *Ionization Based State Read Out of a single Rb-87 Atom*. PhD thesis, 2018.

[21] K. Levenberg. A method for the solution of certain non-linear problems in least squares. *Quarterly of applied mathematics*, 2(2):164–168, 1944.

[22] X.-S. Ma, T. Herbst, T. Scheidl, D. Wang, S. Kropatschek, W. Naylor, B. Wittmann, A. Mech, J. Kofler, E. Anisimova, et al. Quantum teleportation over 143 kilometres using active feed-forward. *Nature*, 489(7415):269, 2012.

[23] D. W. Marquardt. An algorithm for least-squares estimation of nonlinear parameters. *Journal of the society for Industrial and Applied Mathematics*, 11(2):431–441, 1963.

[24] N. Ortegel. *State readout of single Rubidium-87 atoms for a loophole-free test of Bell's inequalities*. PhD thesis, 2016.

[25] J.-W. Pan, D. Bouwmeester, H. Weinfurter, and A. Zeilinger. Experimental entanglement swapping: entangling photons that never interacted. *Physical Review Letters*, 80(18):3891, 1998.

[26] K. Redeker. *title to be announced*. PhD thesis, 2019.

[27] B. Richards and E. Wolf. Electromagnetic diffraction in optical systems, ii. structure of the image field in an aplanatic system. *Proc. R. Soc. Lond. A*, 253(1274):358–379, 1959.

[28] S. Ritter, C. Nölleke, C. Hahn, A. Reiserer, A. Neuzner, M. Uphoff, M. Mücke, E. Figueroa, J. Bochmann, and G. Rempe. An elementary quantum network of single atoms in optical cavities. *Nature*, 484(7393):195, 2012.

[29] W. Rosenfeld. *Experiments with an Entangled System of a Single Atom and a Single Photon*. PhD thesis, 2008.

[30] W. Rosenfeld, D. Burchardt, R. Garthoff, K. Redeker, N. Ortegel, M. Rau, and H. Weinfurter. Event-ready bell test using entangled atoms simultaneously closing detection and locality loopholes. *Phys. Rev. Lett.*, 119:010402, Jul 2017.

[31] N. Sangouard, C. Simon, H. De Riedmatten, and N. Gisin. Quantum repeaters based on atomic ensembles and linear optics. *Reviews of Modern Physics*, 83(1):33, 2011.

[32] N. Schlosser, G. Reymond, and P. Grangier. Collisional blockade in microscopic optical dipole traps. *Physical review letters*, 89(2):023005, 2002.

[33] N. Schlosser, G. Reymond, I. Protsenko, and P. Grangier. Sub-poissonian loading of single atoms in a microscopic dipole trap. *Nature*, 411(6841):1024, 2001.

[34] D. A. Steck. Rubidium 87 d line data. https://steck.us/alkalidata/rubidium87numbers.pdf Version 2.1.5, 2015.

[35] J. D. Thompson, T. G. Tiecke, A. S. Zibrov, V. Vuletić, and M. D. Lukin. Coherence and raman sideband cooling of a single atom in an optical tweezer. *Physical review letters*, 110(13):133001, 2013.

[36] R. Valivarthi, Q. Zhou, G. H. Aguilar, V. B. Verma, F. Marsili, M. D. Shaw, S. W. Nam, D. Oblak, W. Tittel, et al. Quantum teleportation across a metropolitan fibre network. *Nature Photonics*, 10(10):676, 2016.

[37] U. Vazirani and T. Vidick. Fully device-independent quantum key distribution. *Physical review letters*, 113(14):140501, 2014.

[38] J. Volz. *Atom-Photon Entanglement*. PhD thesis, 2006.

[39] J. Volz, M. Weber, D. Schlenk, W. Rosenfeld, J. Vrana, K. Saucke, C. Kurtsiefer, and H. Weinfurter. Observation of entanglement of a single photon with a trapped atom. *Physical Review Letters*, 96(3):030404, 2006.

[40] M. Weber. *Quantum optical experiments towards atom-photon entanglement*. PhD thesis, 2005.

[41] T. Wilk, S. C. Webster, A. Kuhn, and G. Rempe. Single-atom single-photon quantum interface. *Science*, 317(5837):488–490, 2007.

[42] E. Wolf. Electromagnetic diffraction in optical systems-i. an integral representation of the image field. *Proc. R. Soc. Lond. A*, 253(1274):349–357, 1959.

[43] M. Zukowski, A. Zeilinger, M. A. Horne, and A. K. Ekert. "event-ready-detectors"bell experiment via entanglement swapping. *Physical Review Letters*, 71:4287–4290, 1993.

Danksagung

An dieser Stelle möchte ich allen herzlich danken, die mich während dieser Arbeit unterstützt und begleitet haben:

- Professor Harald Weinfurter für die Chance diese Arbeit in seiner Gruppe anfertigen zu können sowie die freie und angenehme Arbeitsatmosphäre.

- Dr. Wenjamin Rosenfeld für seine Art Wissenschaft und Physik zu leben, dafür, dass er neuen Ideen offen und interessiert gegenüber tritt, für sein offenes Ohr bei Fragen jeglicher Art und für seine außerordentliche Hilfsbereitschaft.

- Daniel Burchardt, Robert Garthoff, Tim van Leent, Kai Redeker und Dr. Zhang Wei für die Einführung in das Experiment, für die fachlichen Diskussionen, für die gemeinsame Zeit im Labor und auf Konferenzen und für die Hilfe beim Programmieren und beim Schreiben dieser Arbeit.

- Martin Zeitlmaier für die nette Aufnahme in seinem Büro.

- Allen Mitglieder der Arbeitsgruppe Weinfurter für die gute gemeinsame Zeit.

- Allen meinen Freunden für die interessante und schöne Zeit während des Physikstudiums, im Besonderen Anna, Margret, Sebastian und Timon.

- Laura für ihre Liebe, Geduld und guten Ideen.

- meinen Eltern, Gudrun und Rainer, für ihre allumfassende Unterstützung meines Studiums und Lebens.

Selbstständigkeitserklärung:

Hiermit erkläre ich, die vorliegende Arbeit selbständig verfasst zu haben und keine anderen als die in der Arbeit angegebenen Quellen und Hilfsmittel benutzt zu haben.

München, den 18. Februar 2019

....
(Paul Koschmieder)